ARTICLE

Nucleocytoplasmic transport rates are regulated by cellular processes that modulate GTP availability

Kelsey L. Scott[1], Charles T. Halfmann[1], Allison D. Hoefakker[1,2], Purboja Purkayastha[3], Ting Ching Wang[3], Tanmay P. Lele[3,4,5], and Kyle J. Roux[1,6]

Nucleocytoplasmic transport (NCT), the facilitated diffusion of cargo molecules between the nucleus and cytoplasm through nuclear pore complexes (NPCs), enables numerous fundamental eukaryotic cellular processes. Ran GTPase uses cellular energy in the direct form of GTP to create a gradient across the nuclear envelope (NE) that drives the majority of NCT. We report here that changes in GTP availability resulting from altered cellular physiology modulate the rate of NCT, as monitored using synthetic and natural cargo, and the dynamics of Ran itself. Cell migration, cell spreading, and/or modulation of the cytoskeleton or its connection to the nucleus alter GTP availability and thus rates of NCT, regulating RNA export and protein synthesis. These findings support a model in which changes in cellular physiology that alter GTP availability can regulate the rate of NCT, impacting fundamental cellular processes that extensively utilize NCT.

Introduction

Separation of cytoplasmic and nucleoplasmic compartments, a distinguishing feature for all eukaryotes, is critical to fundamental cellular processes including genome protection, regulation of transcription and translation, and myriad signaling events. The nuclear envelope (NE), a specialized extension of the endoplasmic reticulum, surrounds the genome with a double-membraned physical barrier compartmentalizing the nucleus from the cytoplasm. Nucleocytoplasmic transport (NCT) occurs through nuclear pore complexes (NPCs) embedded within the NE. NPCs are well-conserved structures capable of permitting regulated transit of cargo as large as ~39 nm (Panté and Kann, 2002) and excluding unregulated transit of molecules larger than ~9 nm (Görlich and Kutay, 1999). Regulated transport through the NPCs depends on importins and exportins (Ding and Sepehrimanesh, 2021). These transport receptors selectively bind to specific cargo and shuttle them through the hydrophobic FG-repeat barrier; the transport culminates in dissociation and release of cargo into the other compartments (Aramburu and Lemke, 2017; Tan et al., 2018). For most cargo regulated by NCT, the binding and/or dissociation of transport receptors to cargo is catalyzed by the small GTPase Ran. Nuclear Ran is primarily bound to GTP while cytoplasmic Ran is primarily

bound to GDP (Mattaj and Englmeier, 1998). There is a steep gradient of nuclear RanGTP compared with the cytoplasm that is required for Ran-dependent NCT (Izaurralde et al., 1997).

The transport of cargo across the NE through NPCs does not directly require energy; however, the maintenance of the Ran gradient is an energy-dependent process (Englmeier et al., 1999; Lyman et al., 2002; Ribbeck et al., 1999; Schwoebel et al., 2002). RanGTP exits the nucleus with exportins and bound cargo as well as with importins as they recycle back to the cytoplasm. Once in the cytoplasm, the Ran converts the bound GTP to GDP in a process facilitated by RanGAP and Ran-binding proteins (Bischoff et al., 1994, 1995; Mahajan et al., 1997; Matunis et al., 1996; Yokoyama et al., 1995). This net flux of Ran out of the nucleus and conversion to RanGDP that occurs as a result of NCT would rapidly deplete the Ran gradient and grind the system to a halt. However, RanGDP is shuttled back into the nucleus by NTF2 (Ribbeck et al., 1998) where it binds the Ran GEF, RCC1, leading to the release of the bound GDP and enabling exchange for the more abundant GTP (Klebe et al., 1995b). The binding affinity of Ran for GTP is lower than for GDP (Klebe et al., 1995b), but the ratio of nuclear GTP:GDP is typically favorable for nuclear Ran to be predominantly GTP bound (Kalita et al.,

[1]Enabling Technologies Group, Sanford Research, Sioux Falls, SD, USA; [2]Basic Biomedical Sciences, Sanford School of Medicine, University of South Dakota, Vermillion, SD, USA; [3]Artie McFerrin Department of Chemical Engineering, Texas A&M University, College Station, TX, USA; [4]Department of Biomedical Engineering, Texas A&M University, College Station, TX, USA; [5]Department of Translational Medical Sciences, Texas A&M University, Houston, TX, USA; [6]Department of Pediatrics, Sanford School of Medicine, University of South Dakota, Sioux Falls, SD, USA.

Correspondence to Kyle J. Roux: kyle.roux@sanfordhealth.org

Kelsey L. Scott and Charles T. Halfmann are co-first authors.

2021). Thus, although GTP hydrolysis by Ran occurs in the cytoplasm and is the primary energy-consuming step in NCT, it is the nuclear pool of GTP that replenishes the gradient of RanGTP.

It has been estimated that ~10^5 NCT events occur per second in a typical mammalian cell (Görlich et al., 2003; Smith et al., 2002) with each event requiring consumption of at least one GTP to recharge the system and maintain the Ran gradient. Many critical cellular processes are GTP-dependent including protein synthesis, microtubule dynamics, DNA and RNA synthesis, vesicle transport, cytoskeletal regulation, and G-protein signaling. Previous studies have explored how variations in the availability and even compartmentalization of GTP can regulate the activity of small GTPases like Rac or Rho, impacting actin dynamics and regulating cellular processes such as the formation of membrane protrusions involved in cell migration (Bianchi-Smiraglia et al., 2021; Wawrzyniak et al., 2013). Similarly, the GTPase dynamin superfamily has been shown to be sensitive to changes in GTP availability, altering cellular membrane dynamics at the cell surface and mitochondria (Boissan et al., 2014). Replenishment of GTP by adding a phosphate to GDP is predominantly enabled by nucleoside diphosphate kinase-mediated phosphate shuttling from ATP (Georgescauld et al., 2020); thus the pools of ATP and GTP are intimately connected. Processes that typically consume substantial amounts of available cellular energy include protein synthesis (Lindqvist et al., 2018), generation of ionic gradients (Harris et al., 2012), as well as maintenance of the cytoskeleton and its use in force generation (DeWane et al., 2021).

Although the energy dependence of NCT is well established, there is little information available as to how physiologically relevant variations in cellular energy and, more specifically, the availability of GTP impact rates of NCT. Here, we employed a live-cell GTP sensor and multiple reporters of NCT, including reporters of the dynamics of Ran itself, to investigate how the rates of NCT are altered by physiologically relevant processes that change GTP availability. Furthermore, we began to explore the biological impacts of altered NCT rates, observing changes in RNA export and protein synthesis, processes that extensively utilize Ran GTPase-dependent NCT.

Results

Modulating GTP availability alters rates of NCT in living cells

To assess how GTP availability impacts NCT, we initially validated our chosen tools to measure GTP levels and NCT rates in live cells. We utilized hTERT-immortalized human diploid fibroblasts (BJ-5ta) throughout these studies unless otherwise indicated. To assess NCT, we employed the live-cell light-inducible nuclear localization signal (LINuS) reporter that enables measurement of nuclear import and export rates (Niopek et al., 2014). LINuS is based on a fusion between mCherry and a strong Importin α1/β1 nuclear localization sequence (NLS) that is caged in an inactive conformation via a light-sensitive LOV2 domain and a weaker yet constitutively active CRM1-mediated nuclear export sequence (NES), leading to cytoplasmic

localization of the reporter (Fig. 1 A). Exposure to 488 nm light reversibly uncages the NLS, enabling the NCT-mediated translocation of the LINuS reporter into the nucleus. The NLS is recaged upon removal of 488 nm light exposure, enabling the constitutively active NES to mediate NCT-based export of the LINuS reporter out of the nucleus (Fig. 1 B). This inducible accumulation and loss of nuclear LINuS can be used to measure active import and export, respectively (Fig. 1 C). We assessed if LINuS negatively impacts NCT due to an increase in cargo competing for importins by overexpressing a GFP fused to three tandem NLS (GFP-NLSx3) that uses the same importins as LINuS and observed no significant change in import or export rates for LINuS, suggesting that expression of LINuS does not appreciably alter NCT (Fig. S1 A). To directly monitor cellular levels of available GTP, we used the live-cell GTP reporter system, GEVAL, which is based on a circularly permutated YFP fused to variable GTP-binding domains (Bianchi-Smiraglia et al., 2017). Binding to GTP changes the fluorescent properties of the YFP, altering the fluorescence intensity when excited at 488 nm but not 405 nm, allowing for ratiometric imaging for evaluating intracellular GTP levels independent of GEVAL expression level. To measure available cellular GTP, we utilized GEVAL30, a GEVAL variant that can bind GTP at physiologically relevant concentrations (Bianchi-Smiraglia et al., 2017, 2021). In preliminary experiments, we compared GEVAL30 with another GTP sensor, GEVAL530, which can measure higher concentrations of available GTP. Since both sensors yielded similar results, we utilized GEVAL30 for all experiments in these studies. To ensure changes in GEVAL fluorescence are GTP-dependent, we also utilized GEVALNull, a control reporter that cannot bind GTP. An additional advantage to the GEVAL system is the ability to measure subcellular concentrations of GTP. Since the nuclear pool of GTP is utilized to maintain the Ran gradient, we measured GEVAL intensity in the nucleus. To validate these tools, we reduced intracellular GTP levels with mycophenolic acid (MPA; Fig. 1, D and E), which blocks GTP precursor synthesis but retains the purine salvage pathway, thus it does not fully deplete cellular GTP (Ransom, 1995). GTP depletion by MPA resulted in a considerable decrease in NCT as measured with LINuS, which could be rescued by guanosine supplementation (Fig. 1 F). We next sought to test if increased availability of cellular GTP would alter NCT; however, to our knowledge, there are no reported approaches to directly increase levels of available GTP as there are no known mechanisms by which GTP can be transported into the cell. Therefore, we sought to elevate levels of intracellular GTP by inhibiting a major GTP-consuming process. To this end, we used cycloheximide to inhibit protein synthesis, a cellular process that consumes considerable GTP (Lindqvist et al., 2018) and observed an increase in GTP levels (Fig. 1, G and H) as well as rates of NCT (Fig. 1 I). We also confirmed that ATP depletion profoundly reduced rates of NCT (Fig. 1 J), as previously reported (Schwoebel et al., 2002). Collectively, these experiments align with prior studies on the bioenergetic dependence of NCT, validate our use of GEVAL and LINuS to monitor available cellular GTP and rates of NCT, and that inhibiting a cellular process that directly consumes GTP can enhance the rate of NCT.
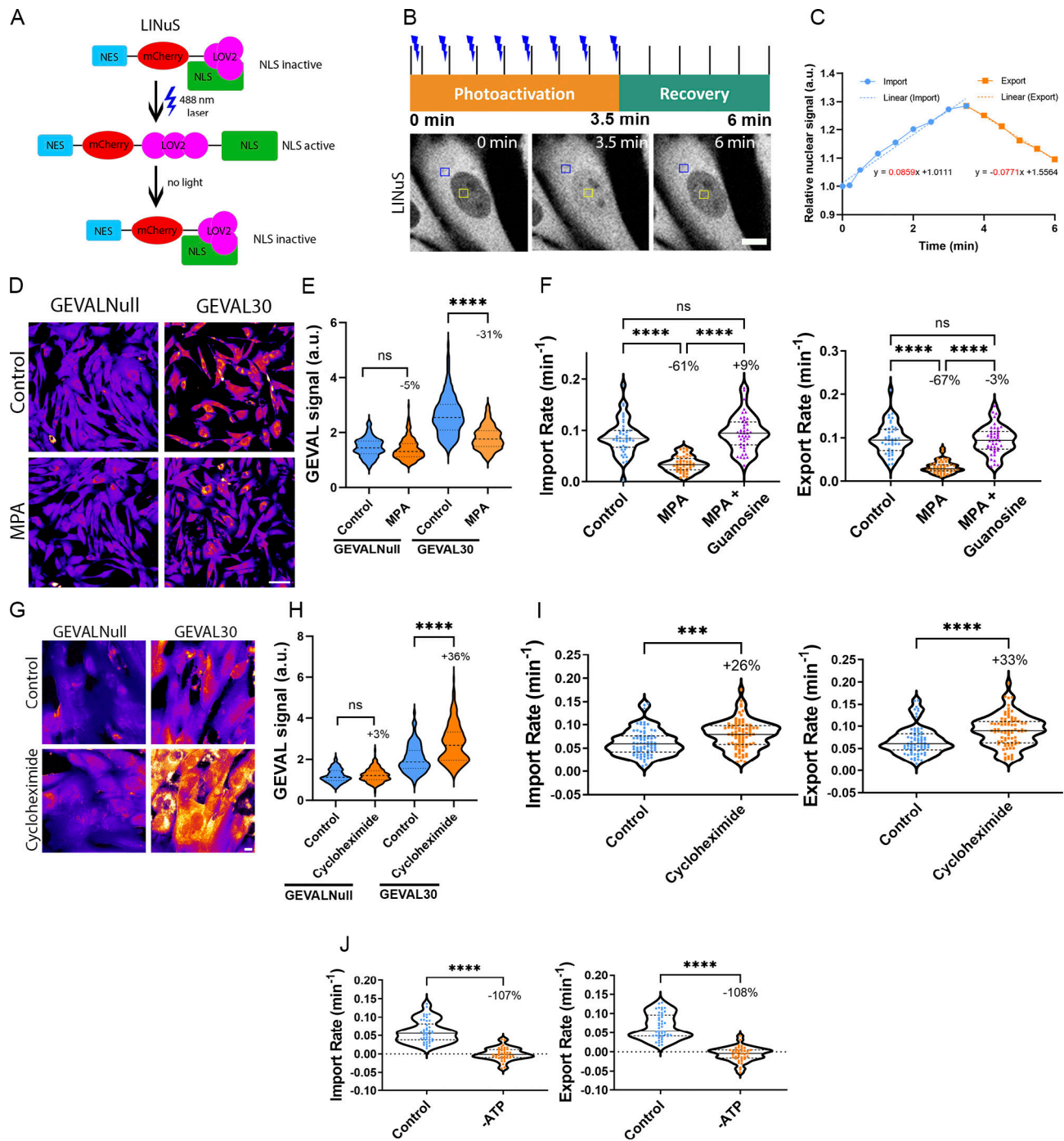
Scott et al.
GTP availability regulates nuclear transport rates

Journal of Cell Biology 2 of 22
https://doi.org/10.1083/jcb.202308152

Figure 1. **Nucleocytoplasmic transport rates are sensitive to levels of GTP. (A)** Model of photoactivatable NCT reporter, LINuS. **(B)** Timeline of LINuS photoactivation and recovery, with representative IF images in BJ-5ta cells stably expressing LINuS during photoactivation and recovery. Yellow and blue boxes denote areas of nuclear and cytoplasmic measurement, respectively. **(C)** Representative graph of LINuS nuclear localization with trend lines, the slopes of which provide import or export rates. **(D)** Ratiometric images (405 nm/488 nm) of BJ-5ta cells expressing either GEVALNull or GEVAL30 treated with MPA. **(E)** Quantification of the GEVAL ratiometric signal (405 nm/488 nm) for each cell expressing GEVALNull (control n = 186, MPA n = 223) or GEVAL30 (control n = 175, MPA n = 264). Results are from two independent replicates. **(F)** Import and export rates of BJ-5ta cells expressing LINuS treated with MPA to deplete GTP (control n = 43, MPA n = 43), then rescued with guanosine supplementation (MPA + guanosine n = 44). Results are from two independent replicates. **(G)** Ratiometric images (405 nm/488 nm) of BJ-5ta cells expressing either GEVALNull or GEVAL30 treated with cycloheximide. **(H)** Quantification of cells from G (GEVALNull control n = 203, cycloheximide n = 232, GEVAL30 control n = 197, cycloheximide n = 198; three independent experiments). **(I)** Import and export rates of BJ-5ta cells expressing LINuS treated with cycloheximide (control n = 74, cycloheximide n = 82; two independent replicates). **(J)** Import and export rates of BJ-5ta cells depleted of ATP with sodium azide and 2-deoxyglucose (control n = 43, -ATP n = 43; two independent replicates). Significance calculated using unpaired t test (E and H–J), one-way ANOVA with Tukey's post hoc (F). ns P > 0.05, P***<0.001, P****<0.0001. Scale bars 10 μm.

Scott et al.
GTP availability regulates nuclear transport rates

Journal of Cell Biology 3 of 22
https://doi.org/10.1083/jcb.202308152

Cell spreading and migration reduce available GTP and rates of NCT

Inhibiting protein synthesis increases available GTP and NCT rates, but this inhibition is unlikely to occur naturally. Next, we assessed if naturally occurring changes in cellular physiology would predictably alter available GTP and thus rates of NCT. A significant portion of cellular energy consumption is for the maintenance and use of the cytoskeleton to generate cellular forces (DeWane et al., 2021). Cells grown on stiffer substrates are typically more spread and generate more cellular tension than those on soft substrates (Solon et al., 2007; Yeung et al., 2005). We grew cells on fibronectin-coated polyacrylamide hydrogels with substrate rigidities of 1, 22, 46, or 308 kPa (Fig. 2 A). The nuclear volumes were similar for cells on all tested substrate rigidities (Fig. 2 B), but cells on 1 kPa substrates were markedly less spread with significantly increased nuclear height compared with those on the stiffer substrates, consistent with previous reports (Fig. 2 C) (Lovett et al., 2013). Cells became increasingly spread as substrate rigidity increased, with the spreading plateauing at 46 kPa (Fig. 2 D). Compared with cells grown on 46 or 308 kPa substrates, cells on both 1 and 22 kPa substrates exhibited significantly elevated levels of GTP (Fig. 2 E) and rates of NCT (Fig. 2 F). To further explore how cell spreading regulates NCT, we rounded the cells by trypsinization, followed by replating to initiate cell spreading. 2 h after plating, cells were attached but rounded compared with 24-hr after plating when cells were spread (Fig. 2, G and H). We observed a profound decrease in NCT in the spread cells at 24 h compared with the rounded cells 2 h after plating (Fig. 2 H). To assess a more physiologically relevant change in cell spreading, monolayers of confluent MCF10A epithelial cells were "scratch wounded" to induce cell migration toward the cell-denuded area (Fig. 2 J) (Tse et al., 2012). Available GTP levels (Fig. 2 K) and NCT rates (Fig. 2 L) were measured in cells 2 h after scratch as they began to migrate into the denuded area (scratch) and compared with cells >600 μm distal from the scratch (middle). Both available GTP and NCT rates were significantly decreased in cells that had flattened out and were migrating into the denuded area compared with those within the monolayer that were less spread or motile. Collectively, these results demonstrate that naturally occurring changes in cell behavior, including spreading induced by substrate rigidity or migration, can alter levels of available GTP and rates of NCT.

Actin and microtubule assembly and their connection to the NE mediate GTP-consuming processes that regulate NCT rates

Changes in cell shape and migration require energy-consuming force-generating structures such as the actin or microtubule networks. Therefore, we explored how perturbation of those structures in spread cells impacts GTP availability and rates of NCT. Depolymerization of actin networks in BJ-5ta cells (Fig. S2 A) with cytochalasin B rapidly increased GTP availability and rates of NCT within 15 min (Fig. 3, A–C). A similar effect on NCT was observed with actin depolymerizing latrunculin B within 10 min (Fig. 3 C). Depolymerization of the microtubule networks with nocodazole (Fig. S2 B) resulted in a similar increase in rates of NCT (Fig. 3 C). Depolymerization of the actin cytoskeleton in

MCF10A cells with cytochalasin B similarly increased available GTP and NCT rates (Fig. 3, D and E). In contrast, perturbation of the vimentin intermediate filament network by siRNA (siVimentin; Fig. S2 C) failed to alter either GTP levels or rates of NCT (Fig. 3, F and G).

We next assessed if the connections between the cytoskeleton and the nucleus participate in the cellular tension-based regulation of NCT. The LINC complex, a primary mediator of these associations (Hoffman et al., 2020; Jahed et al., 2016; Kuhn and Capelson, 2019), can be perturbed by codepletion of SUNs 1 and 2 (Fig. S2 D), which leads to an increase in GTP levels (Fig. 4 A) and rates of NCT (Fig. 4 B). Individual depletion of SUN1 (Fig. S2 E) failed to significantly increase these levels for either, and if anything resulted in a slight reduction in NCT (Fig. 4, A and B), whereas depletion of SUN2 (Fig. S2 F) recapitulated the results of simultaneous codepletion (Fig. 4, A and B). This suggests that in BJ-5ta cells, SUN2 is the primary constituent of the LINC complex that mediates these effects on GTP availability and NCT rates. The impact of LINC complex perturbation on NCT rates was investigated via the expression of a dominant negative lumenal fragment of SUN1 (SS-GFP-SUN1L-KDEL; Fig. S2 G) that outcompetes endogenous SUNs for binding to the KASH-domain nesprin proteins (Crisp et al., 2006). Compared with cells expressing the control (SS-GFP-KDEL), the LINC-perturbed cells exhibited increased rates of NCT (Fig. 4 C). We next assessed the roles of individual nesprins in mediating these LINC complex effects on NCT. Nesprins1 and 2 can be extremely large proteins with a multitude of splice isoforms, but function in part to directly tether the actin cytoskeleton and indirectly tether the microtubules by binding to kinesin and dynein motor proteins to the nucleus (Gundersen and Worman, 2013; Luxton et al., 2010; Zhang et al., 2001). Nesprin3 is a smaller KASH domain protein that binds to the cytolinker plectin and is primarily associated with cytoplasmic intermediate filament association at the nuclear surface (Wilhelmsen et al., 2005). Depletion of either Nesprin1 or 2 using siRNAs (siNesprin1 or siNesprin2, respectively), but not Nesprin3 (siNesprin3; Fig. S2, H–J), increased levels of available GTP (Fig. 4 D) and increased rates of NCT (Fig. 4 E). To control for possible siRNA off-target effects, we performed LINuS experiments using CRISPR interference (KRAB-dCas9-IRES-LINuS) to deplete these proteins (Fig. S3, A–D) and observed similar results as with siRNA-mediated knockdown (Fig. S3, E and F). To further validate that our most frequently used siRNA oligos, those that target siSUN2, have no off-target effects, we overexpressed a V5-tagged mouse SUN2 (V5-SUN2^{Mm}) in BJ-5ta cells expressing LINuS and performed siSUN2 knockdown. Compared with siControl, we observed a partial reduction in SUN2 levels with siSUN2, but no loss of V5 signal, indicating maintenance of mouse SUN2 expression (Fig. S4, A and B). Under these conditions, we observed no significant change in import or export rates (Fig. S4, C and D), suggesting functional rescue of endogenous SUN2. Thus far, we have observed that cell spreading and migration, supported by actin and microtubule networks that are connected to the nucleus via the LINC complex, regulate the levels of available GTP and modulate rates of NCT. These findings are logical and perhaps should be expected
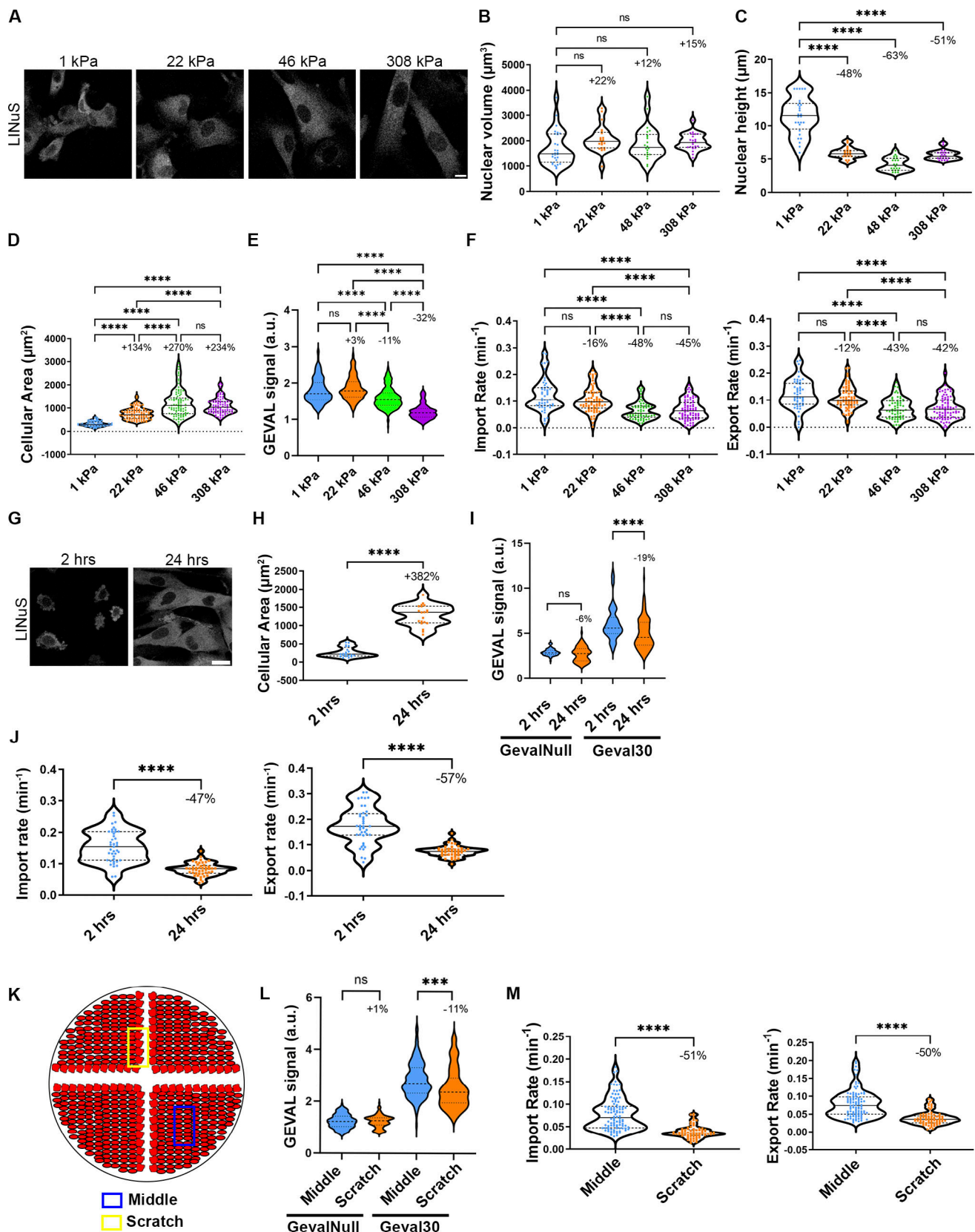
Scott et al.
GTP availability regulates nuclear transport rates

Journal of Cell Biology 4 of 22
https://doi.org/10.1083/jcb.202308152

Figure 2. **Cell spreading regulates levels of GTP and rates of NCT. (A)** Representative confocal images of BJ-5ta cells expressing LINuS plated on poly-acrylamide hydrogels with rigidities of 1, 22, 46, or 308 kPa. **(B–D)** Nuclear volume (1 kPa n = 23, 22 kPa n = 22, 46 kPa n = 21, 308 kPa n = 28; two independent replicates), (C) nuclear height (1 kPa n = 23, 22 kPa n = 22, 46 kPa n = 21, 308 kPa n = 28; two independent replicates), or (D) cellular area (1 kPa n = 81, 22 kPa n = 93, 46 kPa n = 93, 308 kPa n = 93; two independent replicates) of BJ-5ta cells plated on polyacrylamide hydrogels of 1, 22, 46, or 308 kPa rigidities.

(E) Quantification of GEVAL30 signal (405 nm/488 nm) in BJ-5ta cells expressing GEVAL30 in cells plated on polyacrylamide hydrogels at stiffnesses of 1 (n = 152), 22 (n = 178), 46 (n = 197), or 308 kPa (n = 172). Results are from two independent replicates. **(F)** Import and export rates of BJ-5ta cells expressing LINuS plated on polyacrylamide hydrogels with rigidities of 1 (n = 52), 22 (n = 72), 46 (n = 64), or 308 kPa (n = 80) across four independent replicates. **(G)** Representative confocal images of BJ-5ta cells expressing LINuS 2 or 24 h after being plated. **(H)** Cellular area of BJ-5ta cells that had been plated for 2 (n = 20) or 24 h (n = 20) across two independent replicates. **(I)** Quantification of GEVAL signal (405 nm/488 nm) in BJ-5ta cells expressing GEVALNull or GEVAL30 2 h after trypsinization and rounded (2 h, GEVALNull n = 67, GEVAL30 n = 73) or 24 h after trypsinization and spread (24 h, GEVALNull n = 82, GEVAL30 n = 118). Results are from two independent replicates. **(J)** Import and export rates of BJ-5ta cells expressing LINuS either 2 or 24 h after being plated (2 h n = 41, 24 h n = 44; two independent replicates). **(K)** Cartoon of MCF10A cells grown into a monolayer, then scratch wounded. Cells were either imaged along the scratch wound (scratch; yellow rectangle) as they migrated into the denuded space or ~600 µm into the monolayer adjacent from the scratch edge (middle; blue rectangle). **(L)** Quantification of GEVAL signal (405 nm/488 nm) in MCF10A cells expressing GEVALNull or GEVAL30 within the monolayer (middle, GEVALNull n = 147, GEVAL30 n = 138) or edge of scratch (scratch, GEVALNull n = 153, GEVAL30 n = 106) 2 h after scratch. Results are from two independent replicates. **(M)** Import and export rates of MCF10A cells expressing LINuS within the monolayer (middle, n = 98) or edge of scratch (scratch, n = 72) 2 h after scratch, across three independent replicates. Significance calculated using unpaired t test (H, I, K, and L), one-way ANOVA with Tukey's post hoc (D–F), or one way-ANOVA with Dunnett's post hoc (B and C). ns P > 0.05, P***<0.001, P****<0.0001. Scale bars 10 µm.

from the perspective of bioenergetics; however, since cell spreading and/or migration can increase forces on the nucleus, they appear to contradict a recent study reporting that NCT is enhanced by increased forces on the nucleus that mechanically dilate NPCs (Andreu et al., 2022). In support of our findings, it has been reported that the translocation capacity of NPCs considerably exceeds the actual rates of NCT and hypothesized that transportin-cargo binding and/or release, and not the size or permeability of the NPCs, is the primary rate-limiting step in NCT (Ribbeck and Görlich, 2001). To ensure that our discrepant findings are not an artifact of the LINuS reporter, we utilized methods similar to those in the prior study (Andreu et al., 2022), namely transient transfection of LINC perturbing GFP-KASH in mouse embryonic fibroblasts (MEFs) (Fig. S5 A), expressing an alternate photoactivatable NCT reporter called LEXY (Niopek et al., 2016). We observed that LINC perturbation resulted in enhanced export of LEXY, similar to our findings with LINuS, and a non-significant trend toward an increase in import (Fig. S5, B–D). Collectively, these results support a model for adherent spread cells in which cell–substrate interactions and the actin and microtubule networks and their connection to the nucleus enable the generation of cellular forces that consume energy such that levels of GTP, and thus, rates of NCT are reduced.

Conditions that alter GTP availability similarly change rates of induced glucocorticoid receptor import

To expand our findings beyond the more artificial reporters of LINuS or LEXY that rely on minimal NLS and NES sequences specific to importin α/β and Crm1-mediated NCT and to assess if the impacts of altered GTP on NCT rates are specific to transport of those reporters, or instead more globally impact Ran-mediated transport, we utilized inducible import of glucocorticoid receptor (GR). GR is a transcription factor whose nuclear import is mediated by Importin7, in contrast to Importin α/β-based for LINuS, and is inducible with dexamethasone (Hakim et al., 2013). GR-GFP was stably expressed in BJ-5ta cells, and nuclear import was induced by exposure to dexamethasone. GR-GFP utilization of an importin distinct from LINuS was confirmed by inhibiting LINuS import with importazole, an inhibitor of importin-β (Fig. 5, A and B), which had no impact on the induced import of GR-GFP (Fig. 5, C and D). Utilizing some of the same modulators of GTP availability, as was done previously with LINuS, we observed a significant increase in GR import

when cells were rounded at 2 h compared with spread at 24 h (Fig. 5 E) or when cells were depleted of SUN2 (Fig. 5 F). These findings support our hypothesis that the impact of GTP availability on NCT is not limited to specific transportins, but is predicted to affect all Ran gradient-dependent NCT.

Changes in available GTP positively correlate with rates of NCT, however, this correlation was not observed in individual cells at steady state

To further explore the relationship between levels of available GTP and rates of NCT, we compared average GEVAL30 measurements and LINuS import rates across all conditions that showed a significant change relative to control. These changes were then normalized to the control condition within each experiment (Fig. 6 A). We observed a positive correlation between these relative values even though GEVAL30 and LINuS measurements were performed in separate populations of cells at different times. This led us to consider if the level of available GTP and rate of NCT was well-correlated within individual cells at steady state. To assess this at the single-cell level, we coexpressed GEVAL30 and LINuS in BJ-5ta cells and performed consecutive analyses for each reporter at steady state in an asynchronous population of cells plated for 48 h, but surprisingly observed no obvious correlation between these two measurements (Fig. 6 B). This suggested to us that either the coexpression of these reporters interfered with their proper function or that there are factors in addition to the availability of GTP that impact the rate of NCT within a cell. To test if both reporters function appropriately when coexpressed, we performed consecutive measurements of the reporters in cells before and after treatment with cytochalasin B, which rapidly led to an increase in GTP availability and rates of NCT. We observed that average measurements of available GTP and NCT shifted as expected from our results with cells expressing a single reporter, suggesting that coexpression of the reporters did not interfere with their function (Fig. 6 C and inset). We next examined how each cell individually responded to cytochalasin B treatment and observed that the vast majority showed the anticipated shift toward elevated available GTP and increased NCT as would be expected from the population shift (Fig. 6 D). We hypothesized that the minority of cells that failed to show this correlation may have started with elevated levels of available GTP, rates of NCT, or both at steady state prior to cell rounding with cytochalasin B.
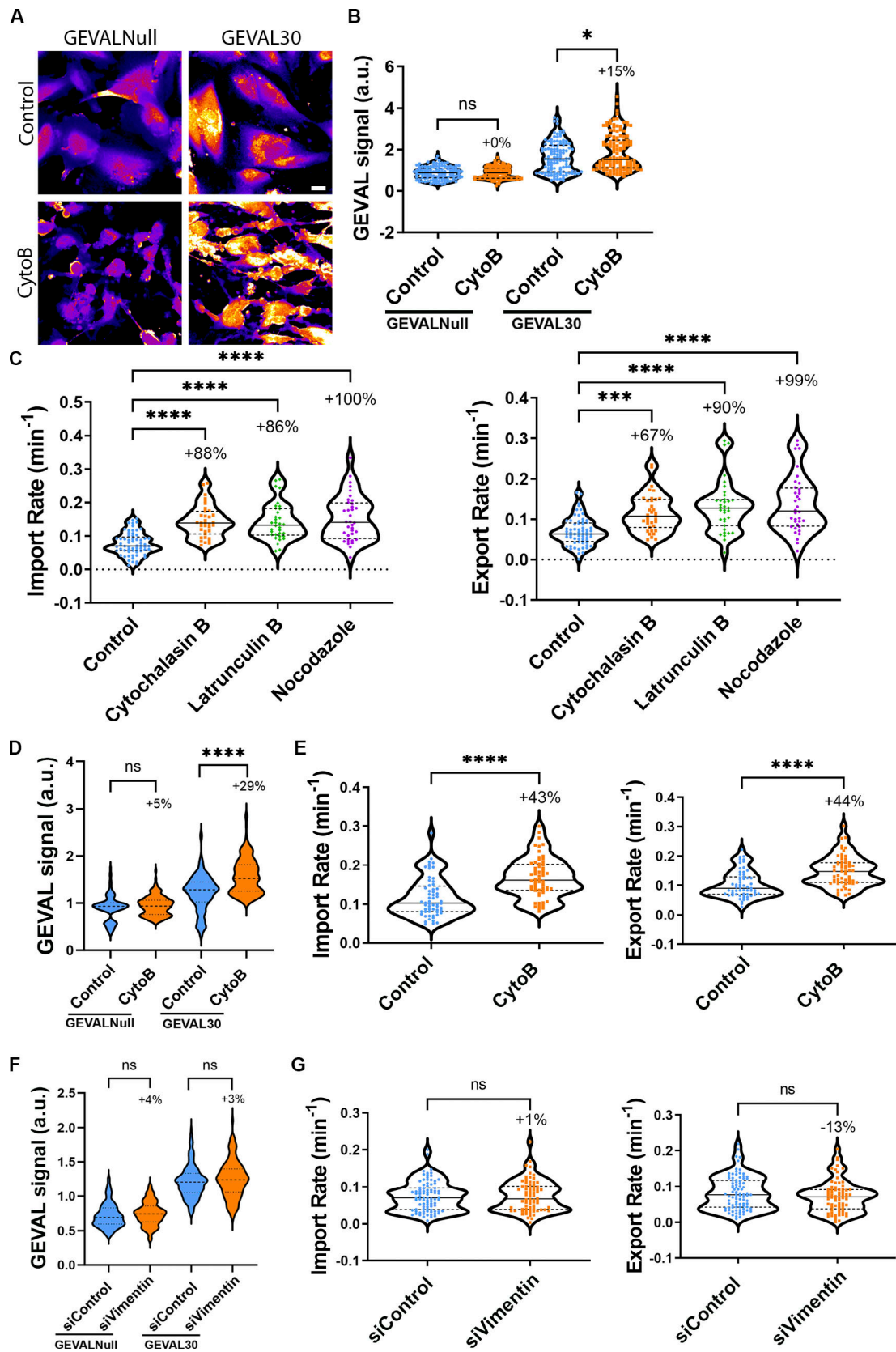
Figure 3. Disruption of actin and microtubule cytoskeleton enhances GTP availability and rates of NCT. (A) Representative ratiometric images (405 nm/488 nm) of BJ-5ta cells expressing either GEVALNull or GEVAL30 treated with cytochalasin B. **(B)** Quantification of GEVAL ratiometric signal (405 nm/488 nm) in BJ-5ta cells expressing GEVALNull or GEVAL30 treated with cytochalasin B (GEVALNull control and cytochalasin B, $n = 121$ and $n = 135$, respectively; GEVAL30 control and cytochalasin B, $n = 117$ and $n = 130$, respectively. Results are from two independent replicates. **(C)** Import and export rates of BJ-5ta cells expressing

LINuS treated with cytochalasin B, latrunculin B, or nocodazole (control $n = 65$, cytochalasin B $n = 35$, latrunculin B $n = 34$, nocodazole $n = 36$). Results are from three independent replicates. **(D)** Quantification of GEVAL ratiometric signal (405 nm/488 nm) in MCF10A cells expressing GEVALNull or GEVAL30 treated with cytochalasin B (GEVALNull control and cytochalasin B, $n = 101$ and $n = 123$, respectively; GEVAL30 control and cytochalasin B, $n = 134$ and $n = 157$, respectively). Results are from three independent replicates. **(E)** Import and export rates of MCF10A cells expressing LINuS treated with cytochalasin B (control $n = 60$, cytochalasin B $n = 60$; results from three independent replicates. **(F)** Quantification of GEVAL ratiometric signal (405 nm/488 nm) in BJ-5ta cells expressing GEVALNull or GEVAL30 depleted of vimentin (GEVALNull siControl and siVimentin, $n = 128$ and $n = 136$, respectively; GEVAL30 siControl and siVimentin, $n = 179$ and $n = 118$, respectively). Results are from three independent replicates. **(G)** Import and export rates of BJ-5ta cells expressing LINuS depleted of vimentin (siControl $n = 89$, siVimentin $n = 74$; three independent replicates). Significance was calculated using unpaired t test (B and D–G), or one-way ANOVA with Dunnett's post hoc (C). ns $P > 0.05$, $P^{***} < 0.001$, $P^{****} < 0.0001$. Scale bar 10 µm.

Indeed, we identified that most of these cells had initial measurements above the 75% quartile for one or both reporters (Fig. 6, E and D, colored lines). Collectively, these results suggest that individual cells in a population exhibit steady-state variations in both available GTP and rates of NCT, but that elevating the availability of GTP will result in an increase in NCT.

Ran GTPase dynamics and localization are modulated by levels of available GTP

To investigate if, in addition to cargo and transportins, Ran GTPase itself exhibits altered rates of nuclear entry and exit based on changes in GTP availability, we examined the dynamics of Ran. We utilized fluorescence loss in photobleaching (FLIP) of cytoplasmic GFP-Ran to measure the subsequent loss of fluorescence from the nucleus, where it predominantly accumulates under normal conditions. We observed a significant increase in the loss of GFP-Ran from the nucleus with conditions that increase GTP availability and rates of NCT, such as SUN2 depletion (Fig. 7, A–C), actin depolymerization (Fig. 7, D and E), cell rounding (Fig. 7, F and G), or inhibition of protein synthesis (Fig. 7, H and I). During the course of the GFP-Ran mobility studies, we observed that the enhanced rate of nuclear exit of Ran driven by elevated levels of GTP coincided with an increase in the steady-state localization of Ran in the cytoplasm. Indeed, we observed that under a prolonged period of enhanced GTP availability and NCT, such as occurs with the depletion of SUN2, total levels of endogenous Ran do not change but Ran is considerably more cytoplasmic (Fig. 8, A–C). Using a more rapid approach to enhance GTP levels by the addition of cytochalasin B, we can also observe an abrupt shift in the localization of endogenous Ran (Fig. 8 D) as well as an exogenous GFP-Ran toward the cytoplasm, both in BJ-5ta (Fig. 8, E–G; and Videos 1 and 2) and MCF10A cells (Fig. 8, H–J) compared with untreated cells. We also observed a rapid shift from cytoplasmic to nuclear localization of GFP-Ran within about 2 h after cell plating that correlated with an increase in cellular spreading area (Fig. 8, K and L). To test if Ran accumulates in the cytoplasm under conditions of enhanced NCT because nuclear reimport by NTF2 is a rate-limiting factor in its nucleocytoplasmic exchange, as has been previously proposed (Ribbeck et al., 1998; Steggerda et al., 2000), we stably overexpressed mCherry-NTF2 and observed a partial rescue of Ran localization following perturbation of the actin cytoskeleton (Fig. 8, M and N) or disruption of the LINC complex (Fig. 8 O). Together, these data suggest that the rates of Ran shuttling between the nucleus and cytoplasm are increased under conditions of enhanced NCT that occurs coincident with elevated GTP.

RNA export and protein synthesis are regulated by altered rates of NCT

Thus far we have demonstrated that naturally occurring or experimentally induced changes in levels of available GTP alter the rates of NCT, but not the outcomes of NCT decisions. We hypothesized that these differences in rates of NCT may have a profound impact on the outcomes of processes that utilize a considerable portion of the cellular transport capacity. RNA export is one such example. Collectively accounting for over 80% of total RNA, rRNA and tRNA utilize Ran-dependent CRM1-mediated nuclear export with the substantially less abundant mRNA predominantly utilizing Ran-independent export pathways (Williams et al., 2018). To assess how altered levels of available GTP modulate the rate of total RNA export, we utilized pulse-chase ethynyl uridine (EU)-based total RNA labeling. After a 1-h labeling, the total level of EU-generated signal enables measurement of RNA synthesis. 3 h after EU washout, the EU signal can be used to assess RNA export from the nucleus by comparing cytoplasmic to nuclear intensity. We first confirmed that blocking CRM1-mediated transport with leptomycin B resulted in an expected shift in RNA localization but not synthesis (Fig. 9, A–C). We next reduced available GTP with MPA and observed a dramatic decrease in RNA export, but not RNA synthesis (Fig. 9, D and E). In contrast, enhancing available levels of GTP by inhibiting protein synthesis resulted in an increase in cytoplasmic RNA but no change in synthesis (Fig. 9, F–H). Similarly, increasing GTP levels by LINC perturbation with SUN2 depletion or depolymerization of the actin cytoskeleton with cytochalasin B both led to an increase in RNA export to the cytoplasm, without a change in levels of RNA synthesis (Fig. 9, I–L). To assess if the steady-state localization of total RNA was altered by enhanced RNA export, we used a live-cell RNA dye and observed a decrease in the ratio of cytosolic to nuclear RNA with inhibition of CRM1-mediated export using leptomycin B or GTP reduction with MPA (Fig. 9, M–O). In contrast, we observed an increase in the cytoplasmic levels of RNA following SUN2 depletion, with no change in total RNA levels for any of these conditions (Fig. 9, P–R).

We next investigated if these changes in cytoplasmic RNA levels that result from altered availability of GTP and rates of NCT impact protein synthesis. Utilizing L-Azidohomoalanine (AHA) labeling of newly synthesized proteins to measure relative rates of overall protein translation, we observed an insignificant trend toward reduction of protein synthesis in cells treated with MPA that reduces available GTP and the expected significant decrease with the protein synthesis inhibitor cycloheximide (Fig. 10, A and B). To confirm that a reduction in NCT,
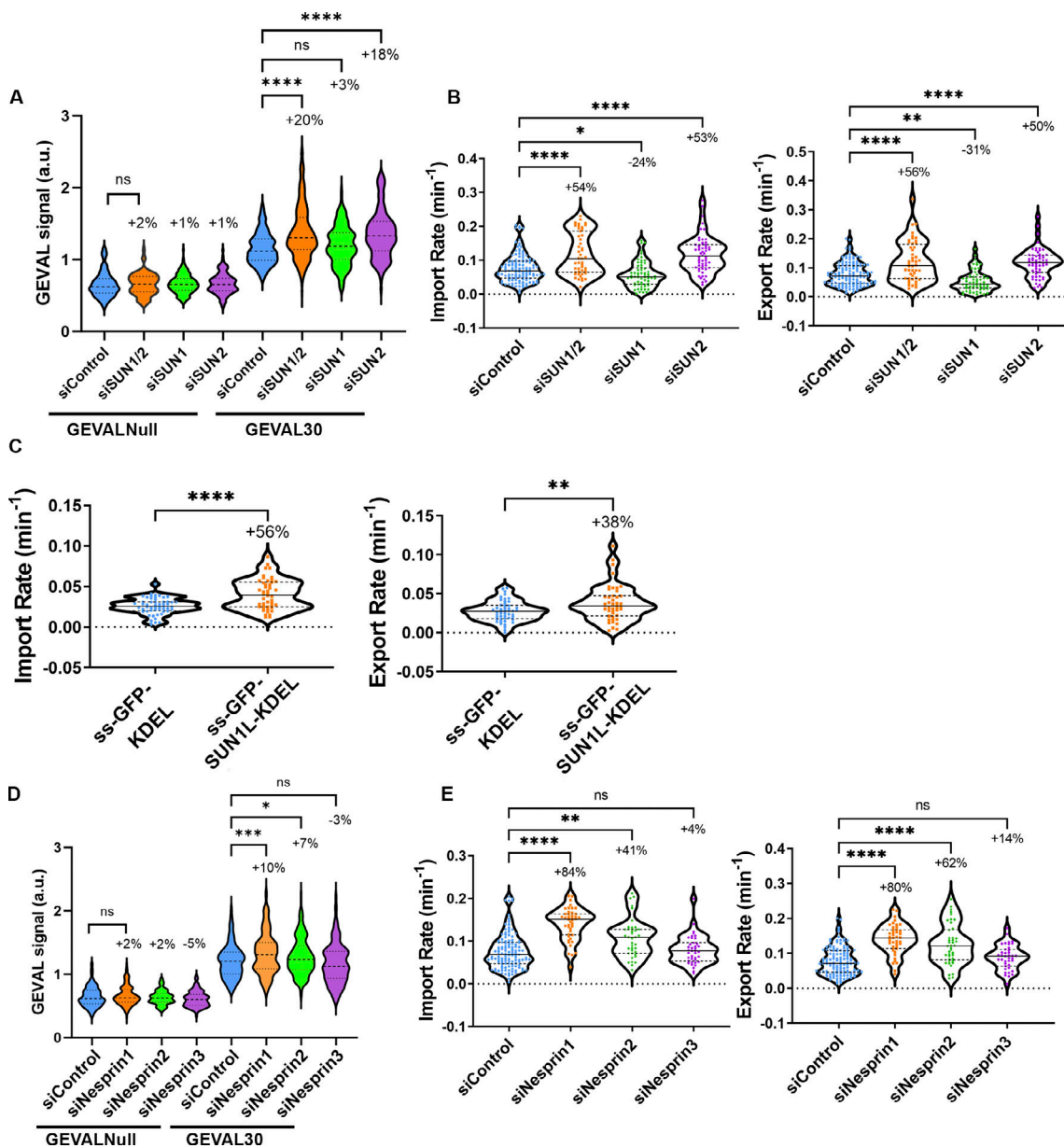
Figure 4. **Disruption of the LINC complex enhances GTP availability and rates of NCT. (A)** Quantification of GEVAL ratiometric signal (405 nm/488 nm) in BJ-5ta cells expressing GEVALnull or GEVAL30 and codepleted of SUN1 and SUN2 (SUN1/2), SUN1, or SUN2 (GEVALNull siControl n = 130, siSUN1/2 n = 115, siSUN1 = 173, siSUN2 = 128. GEVAL30 siControl n = 173, siSUN1/2 n = 203, siSUN1 = 227, siSUN2 = 153). Results are from three independent replicates. **(B)** Import and export rates of BJ-5ta cells stably expressing LINuS and codepleted of SUN1 and SUN2 (SUN1/2), SUN1, or SUN2. siControl n = 125, siSUN1/2 n = 47, siSUN1 n = 61, siSUN2 n = 58. Results are from three independent replicates. **(C)** Import and export rates of MCF10A cells stably expressing LINuS and transiently transfected with ss-GFP-KDEL (n = 53) or ss-SUN1L-GFP-KDEL (n = 46) from three independent replicates. **(D)** Quantification of GEVAL ratiometric signal (405 nm/488 nm) in BJ-5ta cells expressing GEVALnull or GEVAL30 depleted of Nesprin1, Nesprin2, or Nesprin3 (GEVALNull siControl n = 138, siNesprin1 n = 144, siNesprin2 n = 107, siNesprin3 n = 132; GEVAL30 siControl n = 180, siNesprin1 n = 154, siNesprin2 n = 190, siNesprin3 n = 144). Results are from three independent replicates. **(E)** Import and export rates of BJ-5ta cells stably expressing LINuS and depleted of Nesprin1, Nesprin2, or Nesprin3 (si-Control n = 125, siNesprin1 n = 43, siNesprin2 n = 39, siNesprin3 n = 39; three independent replicates). Significance was calculated using t test (C) or one-way ANOVA with Dunnett's post hoc (A, B, D, and E). ns P > 0.05, P*<0.05, P**<0.01, P***<0.001, P****<0.0001.

and specifically CRM1-mediated export, could significantly reduce protein synthesis, we treated cells with leptomycin B and observed a significant reduction in protein synthesis (Fig. 10, C–E). We next assessed how altering cellular processes that regulate the availability of GTP and rates of NCT impact protein synthesis. BJ-5ta cells plated on 1 and 22 kPa substrates had significantly higher levels of protein synthesis compared with

cells plated on 46 and 308 kPa substrates, with decreased protein synthesis plateauing at 46 kPa (Fig. 10 F). Finally, we perturbed the LINC complex by SUN2 depletion and observed a significant increase in protein synthesis (Fig. 10, G and H). These studies collectively suggest that altering the availability of GTP and rates of NCT positively regulate rates of RNA export, cytoplasmic levels of RNA, and the rate of protein synthesis.
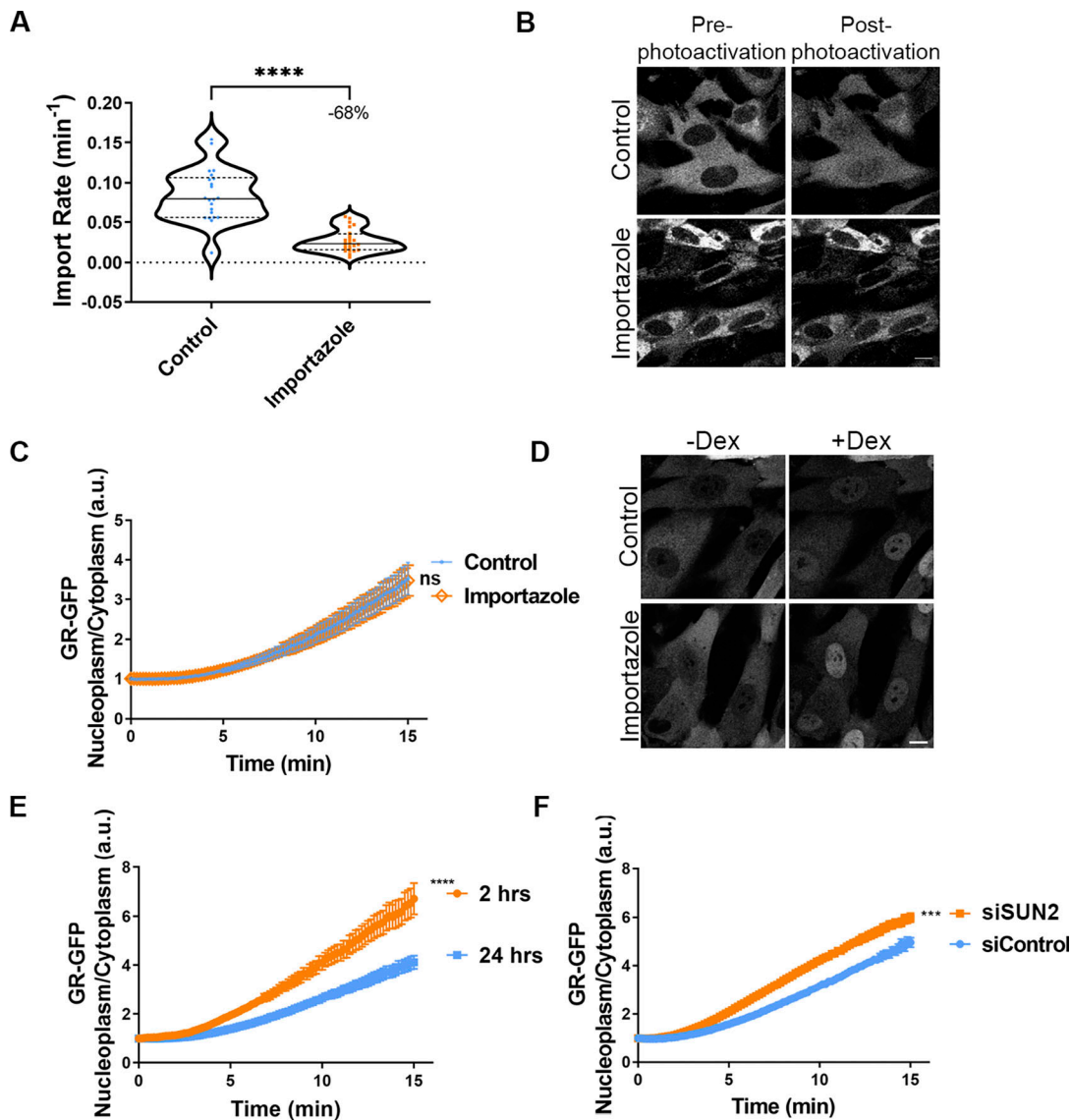
Figure 5. Conditions that alter GTP availability similarly modulate rates of induced GR import. (A) Import rates of BJ-5ta cells expressing LINuS and treated with importazole (control $n = 22$, importazole $n = 24$; two independent replicates). **(B)** Representative confocal images of pre-photoactivation and 3.5 min post-photoactivation of LINuS in BJ-5ta cells treated with importazole. **(C and D)** Quantitative measurements of dexamethasone-induced import of GR-GFP in BJ-5ta cells with or without importazole (Control $n = 22$; importazole $n = 25$; two independent replicates), with representative confocal images (D) of cells with either no dexamethasone treatment (−Dex) or 15 min after dexamethasone treatment (+Dex). **(E and F)** Graphs of dexamethasone-induced nuclear import of GR-GFP in BJ-5ta cells (E) plated for either 2 ($n = 36$) or 24 h ($n = 38$; two independent replicates) or (F) depleted of SUN2 (siControl $n = 105$, siSUN2 $n = 107$; two independent replicates). Significance was calculated using unpaired t test (A, C, E, and F). P***<0.001, P****<0.0001. Scale bars 10 µm. Error bars represent ± SEM.

Discussion

Our studies demonstrate that the rate of NCT is regulated by the availability of GTP. Conditions that elevate levels of free GTP, such as inhibition of protein synthesis, reduced cell spreading, functional disruption of actin or microtubule structures, and/or LINC complex perturbation, all lead to an increase in NCT. These energy-dependent effects on NCT appear generalizable to multiple transportin pathways that utilize Ran and impact the dynamic flow of Ran between the nucleus and cytoplasm. Under all conditions examined, altered levels of GTP preserve the need for signal-induced activation of these NCT pathways. This is evident by the need to stimulate GR import with dexamethasone, even

under conditions with enhanced rates of NCT or the preservation of inducible GR import under conditions of reduced NCT. Based on our observations, it is only the rate of NCT that is altered and not the outcome of a signal to activate transport. However, GTP-dependent changes in the rates of NCT can have profound effects on critical biological processes. A reduction in RNA export, induced by conditions that decrease available GTP, also reduces protein synthesis, not necessarily by limiting cytosolic levels of mRNA that largely uses a Ran-independent export pathway (Köhler and Hurt, 2007), but likely by limiting the Ran-dependent transport of rRNA that comprises ~80% of total RNA (O'Neil et al., 2013) and tRNA that are both needed for
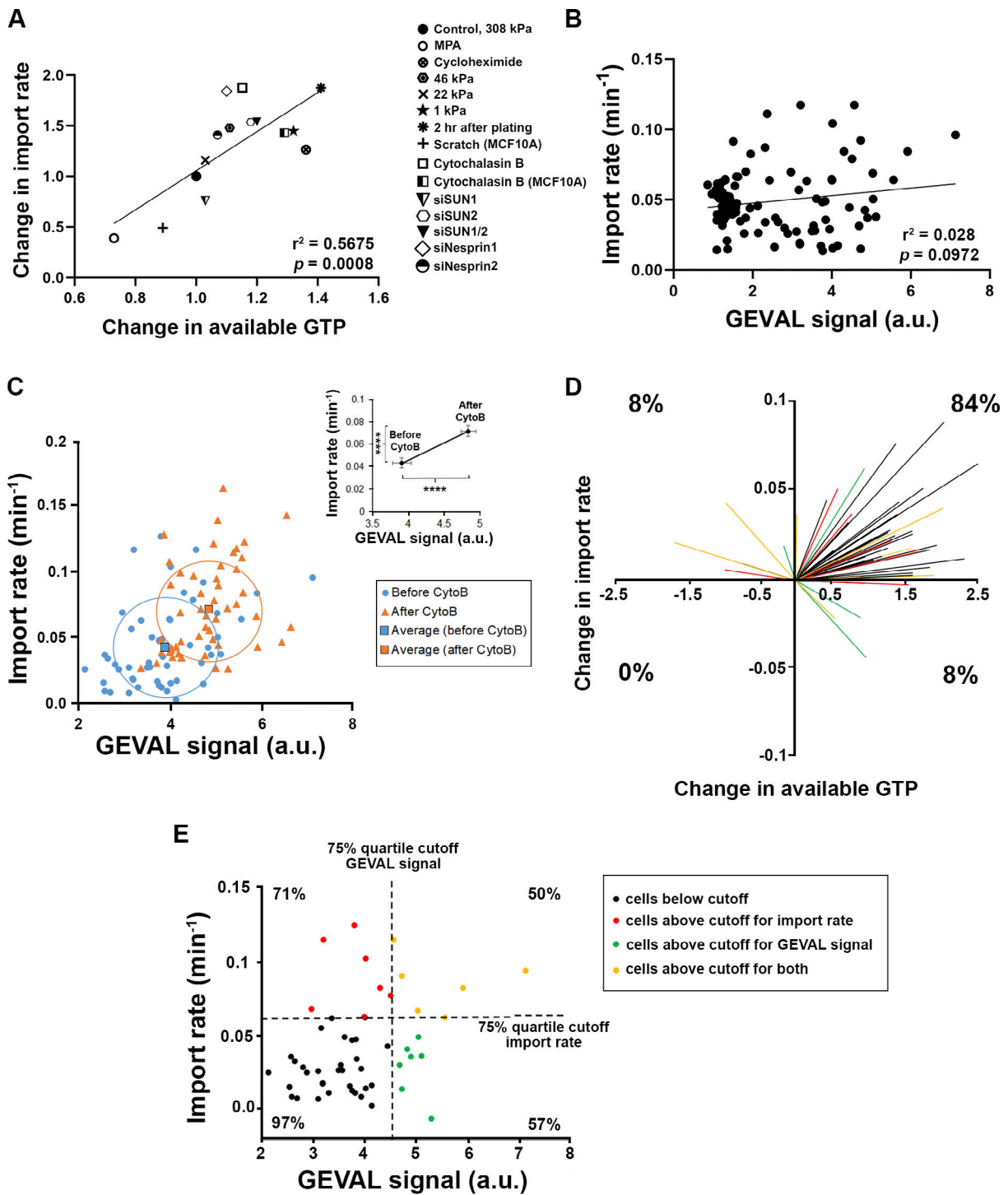
Figure 6. **Changes in available GTP positively correlate with rates of NCT; however, this correlation was not observed in individual cells at steady state. (A)** Correlation between the rate of NCT and available GTP with all treatments used in this study that significantly changed transport. All treatments are from BJ-5ta cells unless noted. **(B)** Plot of import rate and available GTP in BJ-5ta cells stably coexpressing LINuS and GEVAL30 at steady state. Results are from four independent experiments ($n = 128$). Pearson's correlation is annotated for both A and B. **(C)** Measurements of NCT and GTP availability in individual BJ-5ta cells coexpressing LINuS and GEVAL30 before treatment (blue) and 10 min after cytochalasin B treatment (orange). Squares indicate the average GEVAL30 and import rate for each condition, with large unfilled circles highlighting the general distribution of cells within each treatment. Inset shows average NCT rate and GEVAL30 signal before and after cytochalasin B treatment in C. Results are from two independent experiments ($n = 52$). Significance calculated using a paired t test. P***<0.001, P****<0.0001. Error bars represent ± SEM. **(D)** Data from C was analyzed by normalizing the starting point for each cell to 0, with the length and direction of the lines indicating the extent of change. Colors of individual cell trajectories are defined in E. The percent of cells within each quadrant is indicated. **(E)** Cells in C prior to cytochalasin treatment were binned based on their GEVAL30 values and import rates to indicate cells that, compared to those within the 75% quartile (black), exhibited elevated levels of GEVAL30 (green), import rate (red), or both (orange). The listed percentage in each quadrant indicates the percent of cells within that quadrant that exhibited an increase in both GEVAL30 and import rate following cytochalasin b treatment. The measurements of those cells are depicted in the top right quadrant in D.
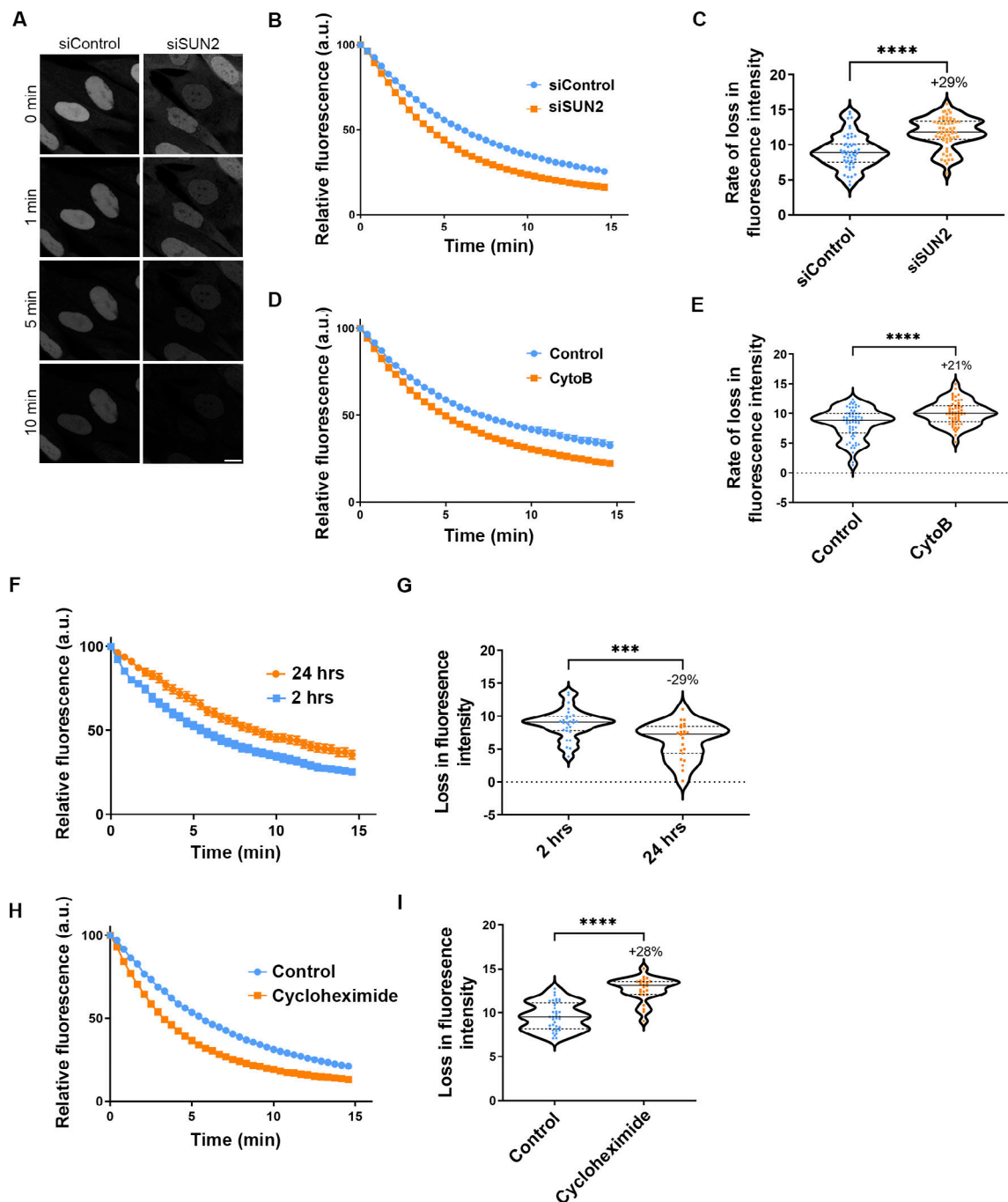
Figure 7. **RanGTPase shuttling between the nucleus and cytoplasm is enhanced by conditions that increase available GTP. (A)** Representative confocal images of GFP-Ran cells depleted of SUN2, where FLIP was used to bleach the cytoplasm and measure the loss of fluorescence intensity from the nucleus. **(B–I)** Graphs of fluorescence change during FLIP (B, D, F, and H) and rate of loss in fluorescence of GFP-Ran over the first 5 min (C, E, G, and I) for cells depleted of SUN2 ([B and C] siControl n = 51, siSUN2 n = 58; three independent replicates), (D and E) treated with cytochalasin B (control n = 64, cytoB n = 60; three independent replicates), (F and G) plated for 2 or 24 h (2 h n = 23, 24 h n = 28; three independent replicates), or (H and I) treated with cycloheximide (control n = 38, cycloheximide n = 26; two independent replicates). Significance was calculated using unpaired t test (C, E, G, and I). P***<0.001, P****<0.0001. Scale bar 10 µm. Error bars represent ± SEM.

ribosome function and thus protein synthesis. This suggests a possible regulatory feedback loop in which the sensitivity of Ran-mediated transport to GTP levels may function to decrease RNA export and protein translation, a process that substantially consumes cellular GTP (Lindqvist et al., 2018), as a GTP-preserving mechanism within the cell during brief periods of reduced energy levels. However, at this time we cannot rule out

that the altered levels of GTP directly impact protein synthesis, although we can demonstrate that direct inhibition of NCT, specifically inhibition of CRM1-mediated export, inhibits protein synthesis without altering available GTP.

We have demonstrated that GTP availability under normal physiological conditions can be a rate-limiting step for NCT, as has been predicted (Görlich et al., 2003). Impairment of GTP- or
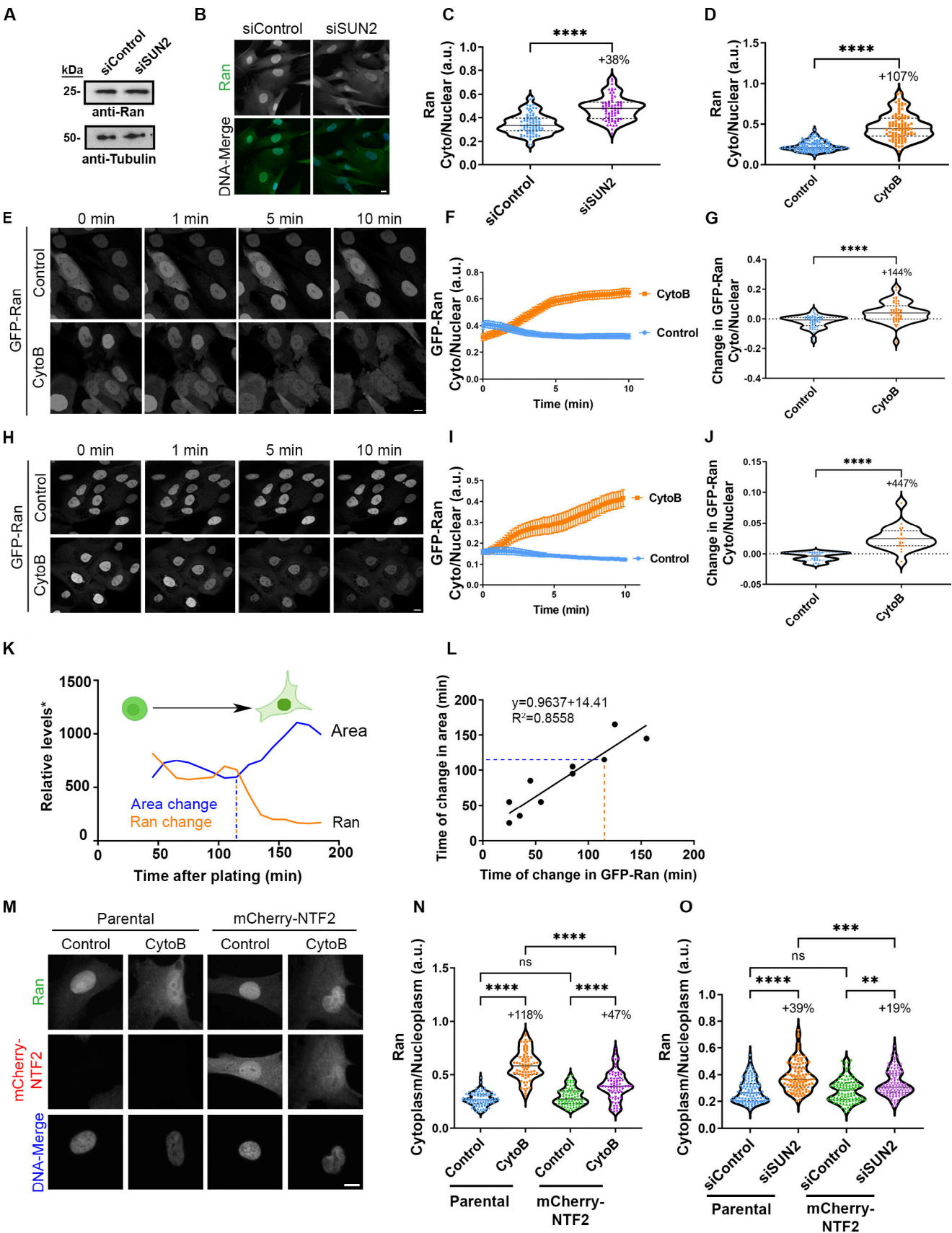
Figure 8. **RanGTPase exhibits increased cytoplasmic localization under conditions that elevate levels of available GTP which can be partially reversed by overexpression of NTF2. (A)** Western blot analysis of BJ-5ta cells depleted of SUN2 and probed for Ran. Tubulin was used as a loading control.

Scott et al.
GTP availability regulates nuclear transport rates

Journal of Cell Biology   13 of 22
https://doi.org/10.1083/jcb.202308152

(B) IF images of SUN2-depleted BJ-5ta cells were probed for Ran (green) and stained with Hoechst (blue) to visualize the nucleus. **(C)** Quantification of cytoplasmic to nuclear ratio of endogenous Ran from BJ-5ta cells treated with siSUN2 (siControl n = 80, siSUN2 n = 69; three independent replicates). **(D)** Quantification of cytoplasmic to nuclear ratio of endogenous Ran in BJ-5ta cells treated with cytochalasin B (control n = 130, CytoB n = 99; three independent replicates). **(E)** Representative confocal images of BJ-5ta cells stably expressing GFP-Ran treated with cytochalasin B at indicated time points. Images taken from Videos 1 and 2. **(F and G)** Quantification and (G) relative rate of change in nuclear to cytoplasmic ratio of GFP-Ran of BJ-5ta cells within the first 2 min of cytochalasin B treatment (control n = 47, CytoB n = 46; three independent replicates). **(H)** Representative confocal images of GFP-Ran in MCF10A cells treated with cytochalasin B at indicated time points. **(I and J)** Quantification (I) and relative change (J) in cytoplasmic to nuclear ratio of GFP-Ran in MCF10A cells treated with cytochalasin B (control n = 60, cytoB n = 60; three independent replicates). **(K)** BJ-5ta cells expressing GFP-Ran were trypsinized and plated on fluorodishes for live cell imaging. Representative graph of the relative levels of GFP-Ran and cellular area over time in a single BJ-5ta GFP-Ran cell. The point at which the cellular area or GFP-Ran localization dramatically changes from initial plating is identified as the time of change (indicated with dashed lines). *In order to combine these measurements on a similar scale, cellular area is represented in pixels and Ran localization change is represented by fluorescence (a.u. × 1,000). **(L)** Correlation of time of change in GFP-Ran to change in cellular area from (K; n = 18 across two independent experiments). Cells with no change in cellular area were not included in linear regression. **(M)** Representative IF images of BJ-5ta parental or mCherry-NTF2 (red) overexpressing cells treated with cytochalasin B and probed for Ran (green). **(N)** Quantification of endogenous cytoplasmic to nuclear Ran from M (parental control n = 85, parental cytoB n = 72, mCherry-NTF2 control n = 77, mCherry-NTF2 cytoB n = 73; three independent replicates). **(O)** Quantification of endogenous cytoplasmic to nuclear Ran in parental or mCherry-NTF2 expressing BJ-5tas depleted of SUN2 (parental siControl n = 106, parental siSUN2 n = 99, mCherry-NTF2 siControl n = 104, mCherry-NTF2 siSUN2 n = 105; three independent replicates). Significance calculated using t test (C, D, G, and J), one-way ANOVA with Tukey's post hoc (N and O). ns P > 0.05, P**<0.01, P***<0.001, P****<0.0001. Scale bars 10 µm. Error bars represent ± SEM. Source data are available for this figure: SourceData F8.

ATP-consuming processes, such as cytoskeletal-mediated tension generation (DeWane et al., 2021) or protein translation (Lindqvist et al., 2018), led to enhanced NCT. It is worth noting that since intracellular levels of GTP cannot be directly increased without affecting other biological processes, it cannot be ruled out that changes in these processes could have additional impacts on NCT beyond the modulation of GTP availability. Since GTP can be generated by NDPK phosphate transfer from ATP (Boissan et al., 2009), GTP levels are intimately related to the availability of free ATP (Schwoebel et al., 2002). Thus, it would be expected that any process that alters cellular energetics would impact NCT. We support the model that it is a combination of Ran's reduced affinity to GTP as compared with GDP (Klebe et al., 1995b), the similar affinity of RCC1, Ran's GEF to RanGTP and RanGDP, respectively (Klebe et al., 1995a), and the sheer volume of GTP consumption needed to maintain the Ran gradient, estimated to be in excess of 10^5 molecules of Ran per second that leave the nucleus (Görlich et al., 2003; Smith et al., 2002), collectively contribute to the sensitivity of Ran to fluctuations in levels of free GTP. It is unclear if Ran-mediated NCT is uniquely sensitive or if there are other GTP-dependent processes that are similarly impacted by physiological fluctuations in free GTP levels. It also remains unknown if the transport-independent functions of Ran, such as NE reformation, mitotic spindle assembly, or cytokinesis (Beaudet et al., 2017; Carazo-Salas et al., 2001; Hutchins et al., 2009), are functionally impacted by the relative availability of free GTP in a manner similar to NCT. Our prediction is that cells eventually adapt to an optimal steady-state level of available energy, finding a balance of GTP production sufficient for a sufficient rate of NCT or perhaps altering mitochondrial abundance or glycolytic pathways if available GTP is insufficient. Transient fluctuations in available GTP, for example, due to cell migration or in response to matrix remodeling, would lead to more dramatic and likely acute changes in rates of NCT.

We have found that an elevated rate of NCT correlates with not only increased nucleocytoplasmic shuttling of Ran but also increased levels of cytosolic Ran, presumably due to the inability of NTF2 to reimport RanGDP into the nucleus as rapidly as RanGTP is being removed from the nucleus by recycling importins and exportin-cargo complexes (Beaudet et al., 2017). RanGAP could be a rate-limiting factor for the nuclear recycling of Ran since NTF2 binds to RanGDP but not RanGTP. However, limited RanGTP hydrolysis mediated by cytosolic RanGAP or perhaps simply the binding of RanGTP to the cytosolic RanGAP would be predicted to reduce NCT since exportin-cargo release and importin-cargo binding both depend on the cytosolic conversion of Ran to a GDP bound form and release from the transportin. Additionally, our evidence that NTF2 overexpression at least partially rescues the nuclear enrichment of Ran under normal conditions supports that it is the level of NTF2 that is rate-limiting for the Ran cycle.

Despite there being a relatively strong correlation of available GTP with rates of NCT within cell populations, there appears to be a poor correlation at the level of individual cells. This may point to the likelihood of alternative regulators of Ran-mediated NCT outside of GTP availability, including but not limited to modulation of regulators of Ran GTPase activity, such as RanGAP, RanGEF, or the RanBP proteins. Some of this single-cell level variation could also be cell cycle-dependent as these studies were performed in asynchronous interphase cells. It is also possible that one or both reporters used for these live cell studies have an inherent level of inaccuracy that is effectively washed out in population studies but is visible in steady-state single-cell studies. Regardless of the nominal correlation at the single cell level, exposure to a condition that elevates levels of available GTP predictably leads to an increase in rates of NCT in the vast majority of cells.

Our studies support that rates of NCT are indirectly regulated by cellular forces, in as much as the generation of those forces decreases free GTP. That is not to say that there are no energy-independent mechanisms that regulate NCT, such as has been proposed via the dilation of NPCs (Zimmerli et al., 2021), but that these do not appear to be the primary mechanism by which cellular forces, including those acting on the nucleus, regulate NCT. Our findings differ from previous studies (Andreu et al., 2022; Elosegui-Artola et al., 2017) that report mechanical forces within the cell enhance rates of NCT, hypothesized to be due to
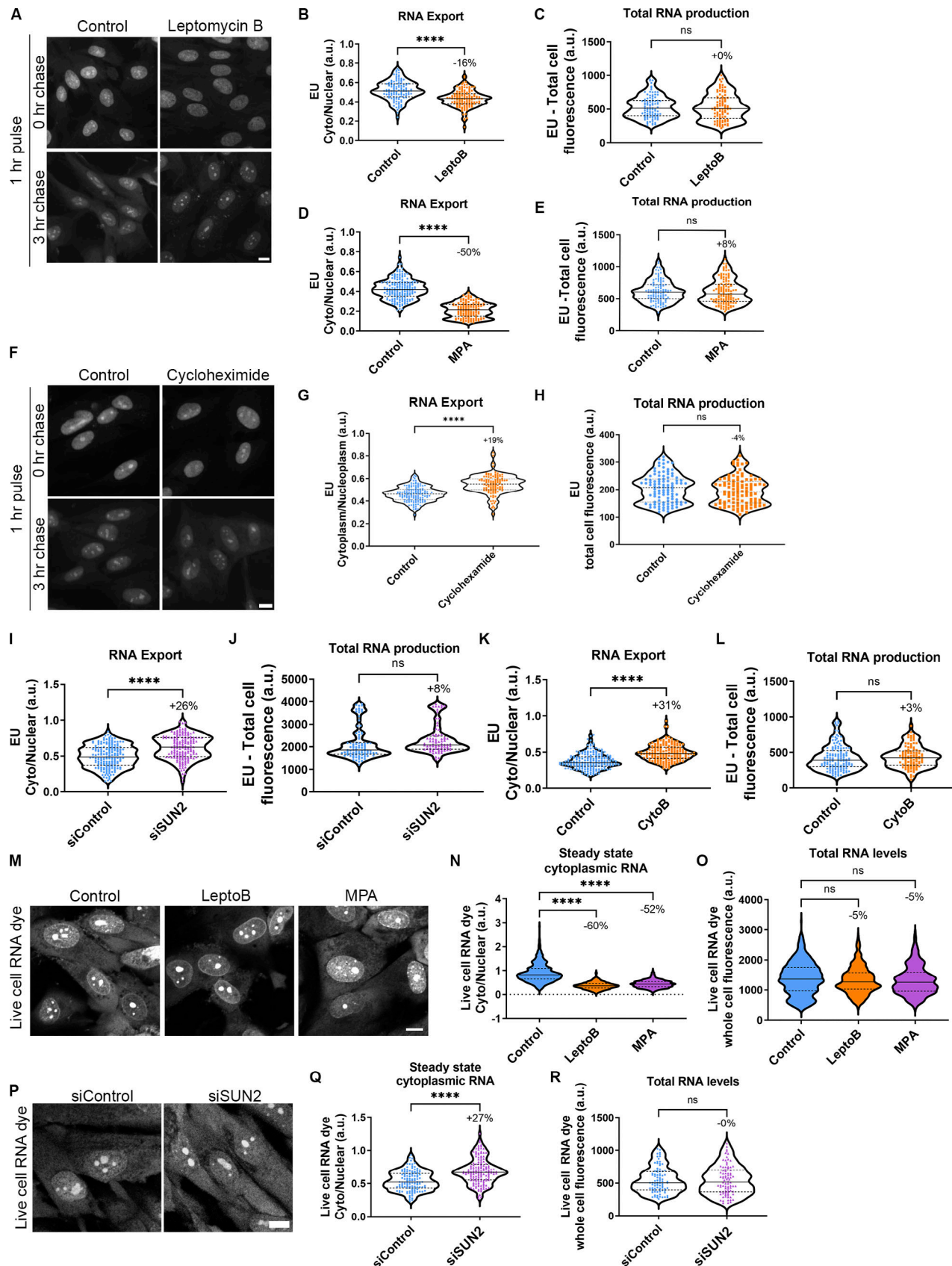
Figure 9. Rates of RNA export and levels of cytosolic RNA are regulated by available GTP. (A) Representative IF images of BJ-5ta cells treated with EU for 1 h (pulse), then re-fed for 0 or 3 h with EU-free media (chase) either untreated (control) or treated with leptomycin B. **(B and C)** Quantification of (B) cytoplasmic to nuclear ratio and (C) total EU labeling of BJ-5ta cells treated with leptomycin B pulsed with EU for 1 h, then chased for 3 h (B; control *n* = 97,

leptomycin B n = 92) or 0 h (C; control n = 119, leptomycin B n = 128). Results are from two independent replicates. **(D and E)** Quantification of (D) cytoplasmic to nuclear ratio or (E) total EU labeling of BJ-5ta cells treated with MPA pulsed with EU for 1 h, then chased for 3 h (D; control n = 178, MPA n = 125) or 0 h (E; control n = 111, MPA n = 125). Each contains two independent replicates. **(F)** Representative IF images of BJ-5ta cells treated with EU for 1 h (pulse), then re-fed for 0 or 3 h with EU-free media (chase) treated with cycloheximide. **(G and H)** Quantification of (G) cytoplasmic to nuclear ratio or (H) total EU labeling of BJ-5ta cells treated with cycloheximide and pulsed with EU for 1 h, then chased for 3 h (G; control n = 146, cycloheximide n = 112) or 0 h (H; control n = 103, cycloheximide n = 106). Each contains two independent replicates. **(I and J)** Quantification of (I) cytoplasmic to nuclear ratio or (J) total EU labeling of BJ-5ta cells depleted of SUN2 pulsed with EU for 1 h, then chased for 3 h (I; siControl n = 175, siSUN2 n = 161) or 0 h (J; siControl n = 92, siSUN2 n = 79). Each contains three independent replicates. **(K and L)** Quantification of (K) cytoplasmic to nuclear ratio or (L) total EU labeling for cytochalsin B-treated BJ-5ta cells pulsed with EU for 1 h, then chased for 3 h (K; control n = 190, CytoB n = 175) or 0 h (L; control n = 140, CytoB n = 103). Each contains two independent replicates. **(M)** Representative confocal images of BJ-5ta cells treated with either MPA or leptomycin B labeled with live cell RNA dye for 1 h. **(N and O)** Quantification of (N) cytoplasmic to nuclear ratio (control n = 582, LeptoB n = 517, MPA n = 409) or (O) total cell fluorescence (control n = 606, LeptoB n = 536, MPA n = 269) across three independent replicates. **(P)** Representative confocal images of BJ-5ta cells depleted of SUN2 labeled with live cell RNA dye for 1 h. **(Q and R)** Quantification of (Q) cytoplasmic to nuclear ratios (siControl n = 122, siSUN2 n = 149) or (R) total cell fluorescence (siControl n = 86, siSUN2 n = 86) of live cell RNA dye in cells depleted of SUN2. Each contains three independent replicates. Significance was calculated using unpaired t test (B–E, G–J, Q, and R) or one-way ANOVA with Dunnett's post hoc (N and O). ns P > 0.05. P****<0.0001. Scale bars 10 μm.

physical stretching of the NPC, and we were unable to explain this discrepancy as we could not replicate those findings using some of the same technical approaches. We did observe that LINC perturbation of cells on stiff surfaces leads to cells behaving similarly to those on soft substrates, but find that the impact on the rate of NCT is the opposite of that reported (Andreu et al., 2022). Based on our findings, we hypothesized that LINC perturbation leads to elevated levels of available GTP and rates of NCT by mechanisms that could include directly interfering with the cytoskeletal dynamics and structure (Lombardi et al., 2011; Sharma and Hetzer, 2023), inhibiting nuclear positioning within the cell during migration (Alam et al., 2015; Gomes et al., 2005; Luxton et al., 2010, 2011; Wu et al., 2014) and/or by inhibiting the motility of the cell (Chancellor et al., 2010; Lombardi et al., 2011; Sharma and Hetzer, 2023). In BJ-5ta cells, we observed that SUN2 appeared to be the primary mediator of the regulation of NCT and GTP availability by the LINC complex as its loss could replicate the loss of both SUNs 1 and 2 or dominant negative perturbation. We also observed in these cells that depletion of SUN1 alone significantly, albeit nominally, reduced the rate of NCT but did not alter the level of GTP. It is possible that the reported colocalization of SUN1 with NPCs (Liu et al., 2007) and its role in interphase NPC assembly (Talamas and Hetzer, 2011) could underly this decrease in NCT. SUN1 has also been reported to modulate the export of mRNA (Li and Noegel, 2015; Li et al., 2017); however, since the majority of mRNA is exported in a Ran-independent manner, this is unlikely to be relevant to the role of the LINC complex in modulating Ran-dependent NCT.

The Ran gradient appears exceptionally sensitive to changes in available GTP, which leads not only to altered rates of NCT but also impacts levels of RNA export from the nucleus and rates of protein synthesis. Bioenergetic regulation of NCT, and thus RNA export and protein synthesis, by titrating the availability of fuel for the Ran gradient is a mechanism by which cells can convert energy fluctuations, including those generated by cellular processes such as migration or spreading, into physiological changes that could impact key processes such as cell cycle, differentiation, and metabolism. It is also tempting to speculate that perhaps some of the defects in NCT that have been reported for various neurodegenerative diseases could be related to altered bioenergetics (Strope et al., 2022), and/or that the altered

bioenergetics that are proposed to underlie several neurodegenerative diseases (Ding and Sepehrimanesh, 2021) could lead to defective NCT as a contributory mechanism of disease. Perhaps post-mitotic cells with a reduced capacity for adaptation would be more sensitive to a bioenergetic decline and be susceptible to reduced NCT.

Materials and methods
Plasmid production
All plasmids were constructed using the Takara Infusion cloning kit. NES-mCherry-LINuS pBabe puro and pBabe neo were constructed using pDN77 (gift from Barbara Di Ventura, University of Freiburg, Freiburg, Germany, and Roland Eils, Berlin Institute of Health, Berlin, Germany; plasmid # 61347; Addgene) as a template amplified with PCR using primers 5′-TGGTACGTAGGA ATTCGCCACCATGCCCAGCACCCGG-3′ and 5′-ATTCCACAGGGT CGACCTAGTCCAGCTTTTTCTTCTTGGCTG-3′. This was recombined with mCherry-NLS pBabe neo (Halfmann et al., 2019) digested with EcoRI and SalI. GFP-KASH4 and a GFP-KASH4 mutant with the last four amino acids of the KASH-domain of mouse nesprin4 replaced with ASAS was constructed as previously described (Roux et al., 2009). GFP-Ran pBabe puro was constructed using human Ran WT cDNA (gift from Brian Burke, A*STAR, Singapore, Singapore) as a template amplified with primers 5′-CTGTACAAGGACCTCGAGGCTGCGCAGGGA-3′ and 5′-ACATTCCACAGGGTCGACTCACAGGTCATCATCC-3′. This was recombined with GFP-BAF pBabe puro (Halfmann et al., 2019) digested with XhoI and SalI. mCherry-NTF2 pBabe neo was constructed using pET23b-NTF2 (gift from Larry Gerace, Scripps Research, La Jolla, CA; plasmid #108918; Addgene) as a template amplified with primers 5′-TCCGGACTCAGATCTCGA GCAATGGGAGACAAGCCAA-3′ and 5′-ATTCCACAGGGTCGA CTCAGCCAAAGTTGTGC-3′. This was recombined with mCherry-NLS pBabe neo digested with XhoI and SalI. GR-GFP pBabe puro was constructed using pk7-GR-GFP (gift from Ian Macara, Vanderbilt University, Nashville, TN; plasmid #15534; Addgene) amplified with primers 5′-AGTGTGGTGGTACGTAGC CACCATGGACTCCAAAGAAT-3′ and 5′-CCGCTCGACGACAGG GGCCCCTTTTGATGAAACAGA-3′. This was recombined with Lap2β-GFP pBabe puro (Halfmann et al., 2019) digested with SnaBI and ApaI. GFP pBabe puro was constructed by amplifying
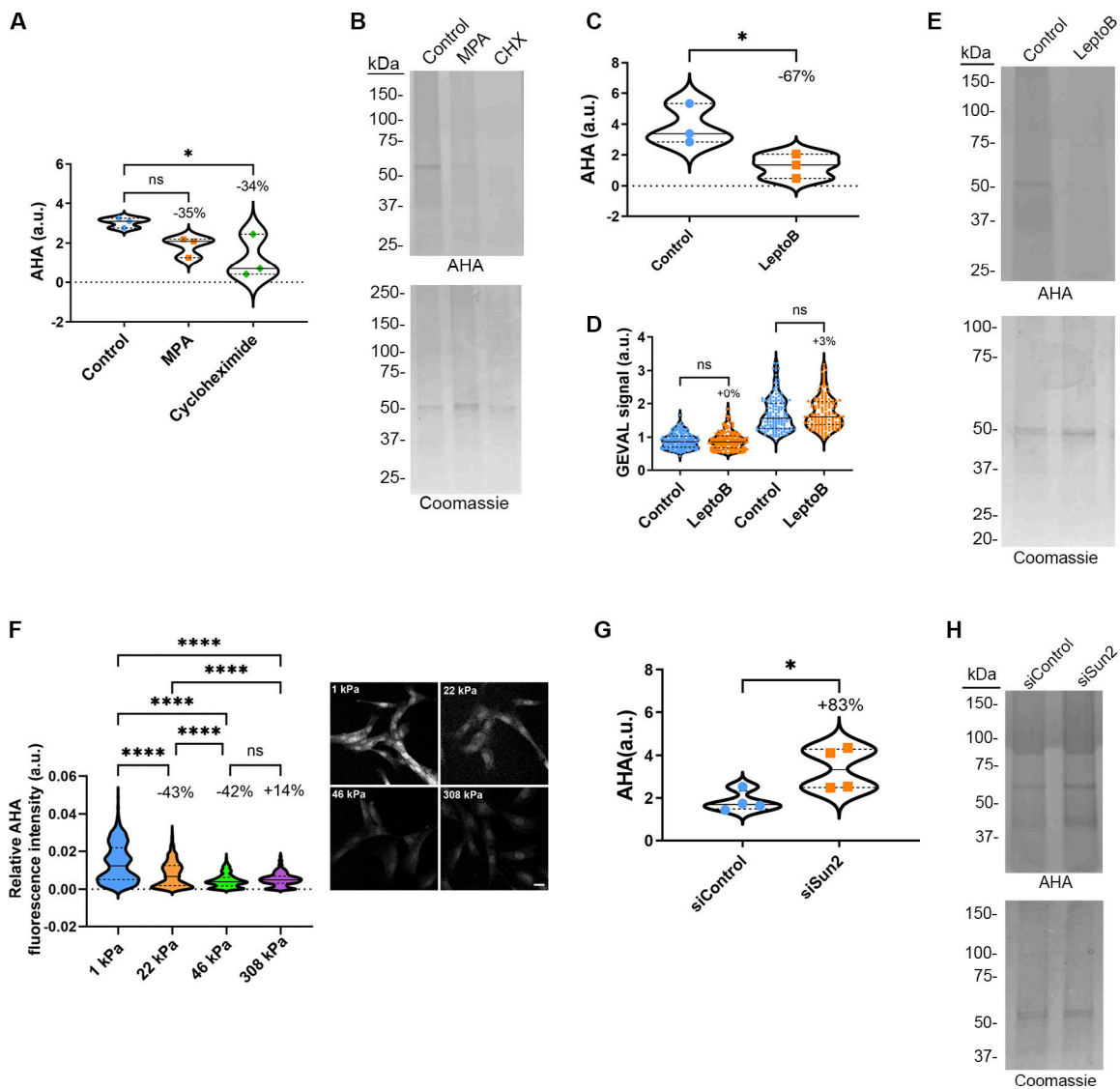
Figure 10. **Rates of protein synthesis are regulated by conditions that alter available GTP. (A and B)** Quantification of protein lysates from AHA-labeled BJ-5ta cells treated with (A) MPA or cycloheximide (CHX) and (B) analyzed by SDS-PAGE. AHA signal was normalized to Coomassie stain. Results are from three independent replicates. **(C and D)** Quantification of protein lysates from AHA-labeled BJ-5ta cells treated with (C) leptomycin B and (D) analyzed by SDS-PAGE. AHA signal was normalized to Coomassie stain. Results are from three independent replicates. **(E)** Quantification of GEVAL ratiometric signal (405 nm/488 nm) in BJ-5ta cells expressing GEVALNull or GEVAL30 and treated with leptomycin B (GEVALNull control $n = 183$, LeptoB $n = 146$; GEVAL30 control $n = 156$, LeptoB $n = 135$). Results are from three independent replicates. **(F)** Quantification of protein synthesis and representative images of BJ-5ta cells plated on increasing substrate rigidities, then fixed and labeled with AHA (1 kPa $n = 646$, 22 kPa $n = 833$, 46 kPa $n = 793$, 308 kPa $n = 530$). Results are from three independent replicates. Scale bar 10 μm. **(G and H)** Quantification of protein lysates from AHA-labeled BJ-5ta cells depleted of (G) SUN2 and (H) analyzed by SDS-PAGE. AHA signal was normalized to Coomassie stain. Results are from four independent replicates. Significance was calculated using one-way ANOVA with Dunnett's post hoc (A), unpaired t test (C, E, and G), or one-way ANOVA with Tukey's post hoc (F). ns $P > 0.05$, P*<0.05. P****<0.0001. Source data are available for this figure: SourceData F10.

GFP with primers 5′-TGGTACGTAGGAATTCTAGCCACCATG GTGAGCA-3′ and 5′-TTACTTGTACAGCTCGTCCATGCCCTCGAG ACATTCCACAGGGTCGAC-3′ and recombined with pBabe puro digested with EcoRI and XhoI. GEVALNull pLVp_puro and GEVAL30 pLVp_puro were gifts from Mikhail A. Nikiforov (Duke University, Durham, NC) (Bianchi-Smiraglia et al., 2017). KRAB-dCas9-IRES-NES-LINuS-mCherry pBabe neo used for CRISPRi-mediated knockdown was constructed using pLX_311-KRAB-dCas9 (a gift from John Doench, William Hahn, and David Root, all at Broad Institute, Cambridge, MA; plasmid #96918;

Addgene) amplified using primers 5′-AGTGTGGTGGTACGTAGC CACCATGGATGCTAAGTCAC-3′ and 5′-CGGAATTGATCCCGC GAATTCTTAGGATCCGCTGCTG-3′. This was recombined into SnaBI and EcoRI digested IRES-NES-LINuS-mCherry pBabe neo. The IRES-NES-LINuS-mCherry pBabe neo backbone vector was created by amplifying an internal ribosome entry site (IRES) from pMSCV-IRES-mCherry-FP (a gift from Dario Vignali, University of Pittsburgh, Pittsburgh, PA; plasmid #52114; Addgene) using primers 5′-AGCATCATGTAAGAATTCGCGGGATCAATT CCG-3′ and 5′-CTTGCTCACCATGTTTAAACTTTATCGTGTT-3′

and recombining into EcoRI digested NES-mCherry-LINuS pBabe neo. The plasmids ss-GFP-L-KDEL and ss-SUN1-L-KDEL pcDNA3.1 were constructed as previously described (Zhang et al., 2019). GFP-NLSx3 pBabe puro was constructed as previously described (Halfmann et al., 2019).

Cell culture

BJ-5ta cells were obtained from American Type Cell Culture (CRL-4001; ATCC) and cultured in Dulbecco's modified Eagle medium (DMEM) with 4.5 g/liter glucose, sodium pyruvate, and L-glutamine (Corning) supplemented with 10% fetal bovine serum (FBS). MCF10A cells were obtained from ATCC (CRL-10317) and cultured in Mammary Epithelial Cell Growth Media (Lonza) supplemented with MEGM Mammary Epithelial Cell Growth Medium BulletKit (Lonza), 10% FBS, and cholera toxin (100 ng/ml). Gentamicin sulfate-amphotericin was omitted from the media. Cells were maintained at 37°C and 5% CO_2. pBabe stable cell lines were generated using retroviral transduction. HEK293 Phoenix cells (CRL-3213; ATCC) were transfected with the plasmid using Lipofectamine 3000 (Thermo Fisher Scientific). The transfected cells were incubated at 37°C for 5 h. The media was changed, and the cells were incubated at 32°C for 48 h. The media was then passed through a 0.45 µM filter onto target cells with polybrene (2.5 µg/ml). After 48 h, either puromycin (0.5 µg/ml; Thermo Fisher Scientific) or G418 sulfate (50 µg/ml; Corning) was added to cells to select for the plasmid of interest. Puromycin was used for pBabe puro plasmids for 2–3 days and G418 sulfate was used for pBabe neo plasmids for 5–7 days. GEVAL stable cell lines were generated by the protocol above using third-generation lentiviral plasmids (CellBio labs) transfected in HEK 293-T cells (CRL-3216; ATCC). All cells were tested monthly for mycoplasma contamination. GFP-KASH4 mutant pcDNA3.1, GFP-KASH4 pcDNA3.1, ss-GFP-KDEL pcDNA3.1, and ss-SUN1L-GFP-KDEL pcDNA3.1 were transiently transfected into cells stably expressing LINuS using Lipofectamine 3000 (Thermo Fisher Scientific) when cells were 80% confluent. Media was changed 6 h after transfection. LINuS studies were performed 48 h after transfection. CRISPRi-mediated depletion of various LINC-complex constituents was performed using a KRAB-dCas9 system (Rosenbluh et al., 2017). Unless otherwise indicated, all experiments were performed on cells 48 h after plating.

Drug treatments

Cells were treated with cytochalasin B (20 µM, 10 min; Tocris Biosciences) and latrunculin B (1 µM, 10 min; MilliporeSigma) to depolymerize actin and with nocodazole (1 µg/ml, 15 min; MilliporeSigma) to depolymerize microtubules. Cells were treated with leptomycin B (20 ng/ml, 48 h; Sigma-Aldrich) to inhibit CRM1-mediated export. Importazole (40 µM, 1 hr; Selleck Chemicals) was used to inhibit Importin β activity. Cells were treated with guanosine (100 µM, 48 hr; TCI America) to supplement GTP synthesis. Cells were treated with cycloheximide (350 µM, 2 hr; Thermo Fisher Scientific) to inhibit protein translation. Cells were treated with MPA (MPA, 1.8 µM, 48 h; Thermo Fisher Scientific) to deplete GTP. Cells were treated with sodium azide (10 mM, 20 min; Sigma-Aldrich) and

2-deoxyglucose (6 mM, 20 min; Sigma-Aldrich) to deplete ATP. Control cells were treated with equal volumes of media. Nuclear import of GR-GFP was induced by the addition of dexamethasone (1 µM, 15 min; Sigma-Aldrich).

Scratch assay

MCF10A cells expressing LINuS, GEVALNull, or GEVAL30 were plated on fluorodishes and allowed to attach for 48 h. A 200-µl pipette tip was then scraped along the bottom of the fluorodish to create a cross-shaped scratch wound in the cell monolayer, followed by a PBS rinse and re-fed with fresh media to remove denuded cells. The cells were allowed to migrate into the denuded area for 2 h prior to imaging.

RNA studies

EU (1 mM; Invitrogen) was incubated with cells in media for 1 h prior to fixation (0 hr chase), or the EU-containing media was replaced, and cells were incubated for 3 h prior to fixation (3-h chase). Cells were fixed with 3% wt/vol PFA in PBS for 10 min and then permeabilized with 0.4% wt/vol Triton-X 100 in PBS for 15 min. EU was visualized using the Click-It cell reaction buffer kit (Invitrogen) and AlexaFluor 488 Azide (Invitrogen) according to the manufacturer's instructions. Cells at 80% confluency were incubated with live-cell RNA dye (Live Cell RNA Imaging Kit, 400X stock; Cell Navigator) for 1 h in media. Images were captured as described below and quantified using ImageJ.

Translation assay

Cells were grown in methionine-free media (Gibco) for 1 h, then AHA was added to the cells for 6 hr. For SDS-PAGE analysis, cells were collected, lysed, sonicated, and the Click-It Protein reaction (Invitrogen) was performed with Tetramethylrhodamine (TAMRA) alkyne (Invitrogen) according to manufacturer's suggestions; however, the methanol precipitation was omitted and samples were analyzed by SDS-PAGE immediately following Click-It labeling. Gel images were acquired on a Licor Odyssey system for AHA fluorescence signal. Subsequently, the gels were stained with Coomassie Brilliant Blue R250 and imaged on a scanner. AHA fluorescence was normalized to Coomassie stain for each sample. For in cellulo AHA labeling, cells were fixed with 3% wt/vol PFA in PBS for 10 min then permeabilized with 0.4% wt/vol Triton-X 100 in PBS for 15 min. AHA was visualized using the Click-It cell reaction buffer kit (Invitrogen) and TAMRA alkyne (Invitrogen) according to manufacturer's instructions. Fixed and labeled cells were imaged on a Nikon A1R confocal microscope (see below for details). Quantification of AHA labeling in fixed cells on substrates was performed with Cell Profiler v 4.2.4, using a pipeline that measured average AHA intensity with Otsu thresholding and a correction factor between 0.5 and 1.0.

siRNA and CRISPRi experiments

siRNA and sgRNA transfections were performed using RNAi-Max (Thermo Fisher Scientific) according to the manufacturer's instructions. Cells were seeded at 70% confluency into 12-well tissue-culture plates containing 1 ml DMEM and allowed to adhere to the bottom of the plate during an overnight incubation at

Scott et al.
GTP availability regulates nuclear transport rates

Journal of Cell Biology   18 of 22
https://doi.org/10.1083/jcb.202308152

37°C. Cells were transfected 24 and 72 h after being seeded, then trypsinized 96 h after being seeded, and replated on FluoroDishes for 48 h prior to imaging. ON-TARGETplus SMARTpool siRNAs (Horizon Discovery) were used to target SUN1 (NM_001130965.3), SUN2 (NM_001199579.2), vimentin (NM_003380.5), nesprin1 (NM_001347701.2), which target isoforms 1, 2, 4, 7, 8, and 11 containing critical KASH and actin-binding domains of nesprin1, nesprin2 (NM_015180.6), which target all 13 isoforms of nesprin2 except for isoform 8 and 9 which lack critical KASH and actin-binding domains and nesprin3 (NM_152592.6). 15 pmol siRNA (0.75 µl of a 20 µM solution in RNase-free H_2O) was used per transfection in all knockdowns. For SUN1/2 codepletion, total siRNA oligo concentration were as described above. CRISPRi guide RNAs (sgRNAs; Horizon Discovery) were used to target canonical promoters of SUN1 (CI-025277-01-0002), SUN2 (CI-009959-01-0002), vimentin (CI-003551-01-0002), Nesprin1 (CI-014039-01-0002), and Nesprin2 (CI-019259-01-0002). CRISPRi-mediated knockdowns were performed using 25 pmol sgRNA (1.25 µl of a 20 µM solution in RNase-free H_2O) per transfection. For SUN1/2 co-depletion and total sgRNA oligo concentration were as described above. All knockdowns for siRNA and CRISPRi were done in parallel with non-targeting control oligos. All siRNA transfections were validated with Western blot analysis or immunofluorescence.

Polyacrylamide substrate synthesis and functionalization

Polyacrylamide gels of four different stiffnesses were synthesized using an established protocol in the literature (Munevar et al., 2001). For obtaining desired stiffness of 1, 22, 46, and 308 kPa, acrylamide (Bio-Rad) and bis-acrylamide (Bio-Rad) were mixed in 50:1, 40:1, 20:1, and 12.5:1 ratios (vol/vol) respectively, to obtain polymer solutions. Polyacrylamide gel solutions were prepared by adding 99.4% vol/vol of polymer solution (of corresponding stiffness) with 0.5% vol/vol ammonium per-sulfate (Thermo Fisher Scientific) and 0.1% vol/vol TEMED (Thermo Fisher Scientific). Each glass-bottomed fluorodish was treated with bind silane for 5 min to make the bottom hydrophilic. 35 µl polyacrylamide gel solution was sandwiched between the hydrophilic fluorodish and a hydrophobic glass coverslip (18 mm diameter) for ~20 min at room temperature to complete the polymerization. After the gel polymerized into a uniform layer, the hydrophobic coverslip was peeled off and the gel was hydrated in PBS for 30 min. Following hydration, the gels coated with Sulfo-SANPAH (G-Biosciences) were functionalized using high-intensity UV for 216 s. The residual Sulfo-SANPAH was removed by washing the gels with PBS three times at room temperature and the gels were further sterilized under low-intensity UV for 30 min. The sterilized gels were coated with fibronectin (10 µg/ml) overnight at 4°C before seeding cells for 24 h prior to imaging.

Immunofluorescence

Cells were grown on glass coverslips and fixed with 3% wt/vol PFA in PBS for 10 min then permeabilized with 0.4% wt/vol Triton-X 100 in PBS for 15 min. Cells were incubated with primary antibodies for 30 min: mouse anti-Ran (1:100, 610341; BD Transduction Laboratories), rabbit anti-Nesprin1 (1:100, HPA019113; Atlas Antibodies), rabbit anti-Nesprin2 (1:50,

HPA003435; Atlas Antibodies), rabbit anti-Nesprin2/4 that detects both Nesprin 2 and 4 (YenZyme; peptide antigen KKAELEWDPAGDIGGLGPLGQ, 1:25, Neelam et al., 2015), Nesprin 2 (MANNES2A, gift from Glenn Morris, Keele University, Keele, UK; 1:100, Randles et al., 2010), and mouse anti-Nesprin3 (1:50, ab123031, 1:50; Abcam) for MEFs, and rabbit anti-Nesprin3 (1:100, HPA077140; Atlas Antibodies) for human cell lines. Primary antibodies were detected with anti-mouse AlexaFluor 488 (1:1,000, A11029; Thermo Fisher Scientific), anti-rabbit Alexa-Fluor 488 (1:1,000, A11034; Thermo Fisher Scientific), and DNA was visualized with Hoescht 33342 (1:5,000). Coverslips were mounted using 10% (wt/vol) Mowiol 4-88 (Polysciences). Fluorescence images were captured using a Nikon Eclipse NiE (40×/0.75 Plan Fluor Nikon objective; 20×/0.75 Plan Apo Nikon objective) microscope at room temperature with a charge-coupled device camera (CoolSnap HQ; Photometrics) linked to a workstation running NIS-Elements software (Nikon). All images were processed in Adobe Photoshop CC 2017 (Adobe) for cropping and brightness/contrast adjustment when applicable.

Western blot

Cells were lysed in SDS-PAGE sample buffer, boiled for 5 min, and then sonicated to shear DNA. Samples were separated on 4–20% gradient gels (Mini-PROTEAN TGX; BioRad) and then transferred to a nitrocellulose membrane. Membranes were blocked using 10% (vol/vol) adult bovine serum and 0.2% TritonX-100 in PBS for 20 min. The membrane was incubated with primary antibodies anti-SUN1 (1:1,000, HPA008346; Atlas Antibodies), rabbit anti-SUN2 (1:1,000, HPA001209; Atlas Antibodies), mouse anti-Vimentin (1:1,000, ab8978; Abcam), mouse anti-Ran (1:5,000, 610341; BD Transduction Laboratories), and mouse anti-tubulin (1:10,000, DM1A; Santa Cruz Biotechnology). Primary antibodies were labeled using goat anti-rabbit HRP (1:10,000, G21234; Thermo Fisher Scientific) and goat anti-mouse HRP (1:10,000, A24524; Thermo Fisher Scientific) and detected using enhanced chemiluminescence via a Bio-Rad ChemiDoc MP System (Bio-Rad). Between each primary antibody, the membrane was quenched using 30% H_2O_2.

Live-cell imaging

LINuS, LEXY, GFP-Ran, GEVAL, and GR-GFP imaging were performed on a Nikon A1R confocal microscope (Plan Apo λ 20×/0.75, Plan Fluor 40×/1.30 Oil DIC H N2, Apo 60×/1.30 Oil λS DIC N2) with a charge-coupled device camera (CoolSnap HQ; Photometrics) linked to a workstation running NIS-Elements software (Nikon) with a heated and CO_2 incubated chamber. Cells were seeded onto 35-mm glass-bottom FluoroDishes (World Precision Instruments) or 8 well glass-bottomed chamber slides (Thermo Fisher Scientific) and were imaged in phenol red-free DMEM supplemented with 10% FBS. Cells were equilibrated in the live cell chamber for 15 min prior to imaging. All images were processed in Adobe Photoshop CC 2017 (Adobe) for cropping and brightness/contrast adjustment when applicable. LINuS cells were allowed to equilibrate in the dark for 10 min prior to activation. LINuS was photoactivated with a 488 nm laser at 100% laser power for 1 s every 30 s for 3.5 min. An image was captured immediately after each photoactivation. For the

recovery stage, images were captured every 30 s for 3 min. Cells that exhibited no import or export of LINuS were excluded from the analysis. Nuclear and cytoplasmic LINuS intensity was measured using ImageJ. The relative nuclear signal was calculated using the ratios of nuclear to cytoplasmic intensity of LINuS cells, and the starting ratios (just prior to photoactivation) were adjusted to 1. Import and export rates were calculated by finding the slope of the line for the activation and recovery phases, respectively, as described in Fig. 1 C. GEVAL images were acquired using dual excitation/emission imaging and capturing images at Ex405/Em530 and Ex488/Em530, as previously described in Bianchi-Smiraglia et al. (2017). ImageJ was used to calculate the mean fluorescence of nuclei within individual cells for each channel. Ratiometric images were generated using the Image calculator function on ImageJ.

FLIP experiments were performed by repeatedly bleaching the cytoplasm of GFP-Ran expressing cells for 1 s immediately followed by image capture every 16 s for 15 min with a 488 nm laser at 100% laser power. The fluorescence intensity of the nucleus and cytoplasm was measured with ImageJ. A non-bleached cell in the same frame was used as a control for photobleaching. Significance was calculated by comparing the rates of fluorescence loss in the first 5 min of photobleaching.

Nuclear shape analysis
Nuclear volume and height measurements were calculated using consecutive confocal Z-stack images of every 0.3 µm of nuclei stained with DAPI using the 60× objective. Nuclear volume measurements were calculated by taking the sum of the area of each stack. The nuclear height was calculated by multiplying the total number of stacks by the distance between each stack.

Statistical analysis
Unpaired t test, one-way ANOVA with Dunnett's post hoc multiple comparison test, or one-way ANOVA with Tukey's post hoc multiple comparison test was used to find significance, as denoted in the figure legends. Outliers were identified prior to analysis using ROUT analysis with Q set to 1%. Graphs with error bars exhibit mean values ± SEM. For violin plots, solid lines represent the median and dashed lines represent quartiles. Percent change represents a comparative change in mean. Statistical analysis, outlier identification, and import and export rates graph generation were performed in GraphPad Prism v.9.5.1 (GraphPad Software, Inc.).

Online supplemental material
Fig. S1 shows assessing the impact of overexpression of an NLS-containing protein on NCT. Fig. S2 shows validation of drug treatments and LINC complex disruption. Fig. S3 shows validation of LINC perturbation on NCT using CRISPR interference. Fig. S4 shows validation of siSUN2 specificity. Fig. S5 shows validation of LINC perturbation on NCT using the LEXY reporter.

Acknowledgments

References

Alam, S.G., D. Lovett, D.I. Kim, K.J. Roux, R.B. Dickinson, and T.P. Lele. 2015. The nucleus is an intracellular propagator of tensile forces in NIH 3T3 fibroblasts. *J. Cell Sci.* 128:1901–1911. https://doi.org/10.1242/jcs.161703

Andreu, I., I. Granero-Moya, N.R. Chahare, K. Clein, M. Molina-Jordán, A.E.M. Beedle, A. Elosegui-Artola, J.F. Abenza, L. Rossetti, X. Trepat, et al. 2022. Mechanical force application to the nucleus regulates nucleocytoplasmic transport. *Nat. Cell Biol.* 24:896–905. https://doi.org/10.1038/s41556-022-00927-7

Aramburu, I.V., and E.A. Lemke. 2017. Floppy but not sloppy: Interaction mechanism of FG-nucleoporins and nuclear transport receptors. *Semin. Cell Dev. Biol.* 68:34–41. https://doi.org/10.1016/j.semcdb.2017.06.026

Beaudet, D., T. Akhshi, J. Phillipp, C. Law, and A. Piekny. 2017. Active Ran regulates anillin function during cytokinesis. *Mol. Biol. Cell.* 28:3517–3531. https://doi.org/10.1091/mbc.e17-04-0253

Bianchi-Smiraglia, A., M.S. Rana, C.E. Foley, L.M. Paul, B.C. Lipchick, S. Moparthy, K. Moparthy, E.E. Fink, A. Bagati, E. Hurley, et al. 2017. Internally ratiometric fluorescent sensors for evaluation of intracellular GTP levels and distribution. *Nat. Methods.* 14:1003–1009. https://doi.org/10.1038/nmeth.4404

Bianchi-Smiraglia, A., D.W. Wolff, D.J. Marston, Z. Deng, Z. Han, S. Moparthy, R.M. Wombacher, A.L. Mussell, S. Shen, J. Chen, et al. 2021. Regulation of local GTP availability controls RAC1 activity and cell invasion. *Nat. Commun.* 12:6091. https://doi.org/10.1038/s41467-021-26324-6

Bischoff, F.R., C. Klebe, J. Kretschmer, A. Wittinghofer, and H. Ponstingl. 1994. RanGAP1 induces GTPase activity of nuclear Ras-related Ran. *Proc. Natl. Acad. Sci. USA.* 91:2587–2591. https://doi.org/10.1073/pnas.91.7.2587

Bischoff, F.R., H. Krebber, E. Smirnova, W. Dong, and H. Ponstingl. 1995. Co-activation of RanGTPase and inhibition of GTP dissociation by Ran-GTP binding protein RanBP1. *EMBO J.* 14:705–715. https://doi.org/10.1002/j.1460-2075.1995.tb07049.x

Boissan, M., S. Dabernat, E. Peuchant, U. Schlattner, I. Lascu, and M.L. Lacombe. 2009. The mammalian Nm23/NDPK family: From metastasis control to cilia movement. *Mol. Cell. Biochem.* 329:51–62. https://doi.org/10.1007/s11010-009-0120-7

Boissan, M., G. Montagnac, Q. Shen, L. Griparic, J. Guitton, M. Romao, N. Sauvonnet, T. Lagache, I. Lascu, G. Raposo, et al. 2014. Membrane

trafficking. Nucleoside diphosphate kinases fuel dynamin superfamily proteins with GTP for membrane remodeling. *Science.* 344:1510–1515. https://doi.org/10.1126/science.1253768

Carazo-Salas, R.E., O.J. Gruss, I.W. Mattaj, and E. Karsenti. 2001. Ran-GTP coordinates regulation of microtubule nucleation and dynamics during mitotic-spindle assembly. *Nat. Cell Biol.* 3:228–234. https://doi.org/10.1038/35060009

Chancellor, T.J., J. Lee, C.K. Thodeti, and T. Lele. 2010. Actomyosin tension exerted on the nucleus through nesprin-1 connections influences endothelial cell adhesion, migration, and cyclic strain-induced reorientation. *Biophys. J.* 99:115–123. https://doi.org/10.1016/j.bpj.2010.04.011

Crisp, M., Q. Liu, K. Roux, J.B. Rattner, C. Shanahan, B. Burke, P.D. Stahl, and D. Hodzic. 2006. Coupling of the nucleus and cytoplasm: Role of the LINC complex. *J. Cell Biol.* 172:41–53. https://doi.org/10.1083/jcb.200509124

DeWane, G., A.M. Salvi, and K.A. DeMali. 2021. Fueling the cytoskeleton: Links between cell metabolism and actin remodeling. *J. Cell Sci.* 134:jcs248385. https://doi.org/10.1242/jcs.248385

Ding, B., and M. Sepehrimanesh. 2021. Nucleocytoplasmic transport: Regulatory mechanisms and the implications in neurodegeneration. *Int. J. Mol. Sci.* 22:4165. https://doi.org/10.3390/ijms22084165

Elosegui-Artola, A., I. Andreu, A.E.M. Beedle, A. Lezamiz, M. Uroz, A.J. Kosmalska, R. Oria, J.Z. Kechagia, P. Rico-Lastres, A.L. Le Roux, et al. 2017. Force triggers YAP nuclear entry by regulating transport across nuclear pores. *Cell.* 171:1397–1410.e14. https://doi.org/10.1016/j.cell.2017.10.008

Englmeier, L., J.C. Olivo, and I.W. Mattaj. 1999. Receptor-mediated substrate translocation through the nuclear pore complex without nucleotide triphosphate hydrolysis. *Curr. Biol.* 9:30–41. https://doi.org/10.1016/S0960-9822(99)80044-X

Georgescauld, F., Y. Song, and A. Dautant. 2020. Structure, folding and stability of nucleoside diphosphate kinases. *Int. J. Mol. Sci.* 21:6779. https://doi.org/10.3390/ijms21186779

Gomes, E.R., S. Jani, and G.G. Gundersen. 2005. Nuclear movement regulated by Cdc42, MRCK, myosin, and actin flow establishes MTOC polarization in migrating cells. *Cell.* 121:451–463. https://doi.org/10.1016/j.cell.2005.02.022

Görlich, D., and U. Kutay. 1999. Transport between the cell nucleus and the cytoplasm. *Annu. Rev. Cell Dev. Biol.* 15:607–660. https://doi.org/10.1146/annurev.cellbio.15.1.607

Görlich, D., M.J. Seewald, and K. Ribbeck. 2003. Characterization of Ran-driven cargo transport and the RanGTPase system by kinetic measurements and computer simulation. *EMBO J.* 22:1088–1100. https://doi.org/10.1093/emboj/cdg113

Gundersen, G.G., and H.J. Worman. 2013. Nuclear positioning. *Cell.* 152:1376–1389. https://doi.org/10.1016/j.cell.2013.02.031

Hakim, A., P.J. Barnes, I.M. Adcock, and O.S. Usmani. 2013. Importin-7 mediates glucocorticoid receptor nuclear import and is impaired by oxidative stress, leading to glucocorticoid insensitivity. *FASEB J.* 27:4510–4519. https://doi.org/10.1096/fj.12-222604

Halfmann, C.T., R.M. Sears, A. Katiyar, B.W. Busselman, L.K. Aman, Q. Zhang, C.S. O'Bryan, T.E. Angelini, T.P. Lele, and K.J. Roux. 2019. Repair of nuclear ruptures requires barrier-to-autointegration factor. *J. Cell Biol.* 218:2136–2149. https://doi.org/10.1083/jcb.201901116

Harris, J.J., R. Jolivet, and D. Attwell. 2012. Synaptic energy use and supply. *Neuron.* 75:762–777. https://doi.org/10.1016/j.neuron.2012.08.019

Hoffman, L.M., M.A. Smith, C.C. Jensen, M. Yoshigi, E. Blankman, K.S. Ullman, and M.C. Beckerle. 2020. Mechanical stress triggers nuclear remodeling and the formation of transmembrane actin nuclear lines with associated nuclear pore complexes. *Mol. Biol. Cell.* 31:1774–1787. https://doi.org/10.1091/mbc.E19-01-0027

Hutchins, J.R., W.J. Moore, and P.R. Clarke. 2009. Dynamic localisation of Ran GTPase during the cell cycle. *BMC Cell Biol.* 10:66. https://doi.org/10.1186/1471-2121-10-66

Izaurralde, E., U. Kutay, C. von Kobbe, I.W. Mattaj, and D. Görlich. 1997. The asymmetric distribution of the constituents of the Ran system is essential for transport into and out of the nucleus. *EMBO J.* 16:6535–6547. https://doi.org/10.1093/emboj/16.21.6535

Jahed, Z., M. Soheilypour, M. Peyro, and M.R. Mofrad. 2016. The LINC and NPC relationship: It's complicated! *J. Cell Sci.* 129:3219–3229. https://doi.org/10.1242/jcs.184184

Kalita, J., L.E. Kapinos, and R.Y.H. Lim. 2021. On the asymmetric partitioning of nucleocytoplasmic transport: Recent insights and open questions. *J. Cell Sci.* 134:jcs240382. https://doi.org/10.1242/jcs.240382

Klebe, C., F.R. Bischoff, H. Ponstingl, and A. Wittinghofer. 1995a. Interaction of the nuclear GTP-binding protein Ran with its regulatory proteins RCC1 and RanGAP1. *Biochemistry.* 34:639–647. https://doi.org/10.1021/bi00002a031

Klebe, C., H. Prinz, A. Wittinghofer, and R.S. Goody. 1995b. The kinetic mechanism of Ran--nucleotide exchange catalyzed by RCC1. *Biochemistry.* 34:12543–12552. https://doi.org/10.1021/bi00039a008

Köhler, A., and E. Hurt. 2007. Exporting RNA from the nucleus to the cytoplasm. *Nat. Rev. Mol. Cell Biol.* 8:761–773. https://doi.org/10.1038/nrm2255

Kuhn, T.M., and M. Capelson. 2019. Nuclear pore proteins in regulation of chromatin state. *Cells.* 8:1414. https://doi.org/10.3390/cells8111414

Lindqvist, L.M., K. Tandoc, I. Topisirovic, and L. Furic. 2018. Cross-talk between protein synthesis, energy metabolism and autophagy in cancer. *Curr. Opin. Genet. Dev.* 48:104–111. https://doi.org/10.1016/j.gde.2017.11.003

Li, P., and A.A. Noegel. 2015. Inner nuclear envelope protein SUN1 plays a prominent role in mammalian mRNA export. *Nucleic Acids Res.* 43:9874–9888. https://doi.org/10.1093/nar/gkv1058

Li, P., M. Stumpf, R. Müller, L. Eichinger, G. Glöckner, and A.A. Noegel. 2017. The function of the inner nuclear envelope protein SUN1 in mRNA export is regulated by phosphorylation. *Sci. Rep.* 7:9157. https://doi.org/10.1038/s41598-017-08837-7

Liu, Q., N. Pante, T. Misteli, M. Elsagga, M. Crisp, D. Hodzic, B. Burke, and K.J. Roux. 2007. Functional association of Sun1 with nuclear pore complexes. *J. Cell Biol.* 178:785–798. https://doi.org/10.1083/jcb.200704108

Lombardi, M.L., D.E. Jaalouk, C.M. Shanahan, B. Burke, K.J. Roux, and J. Lammerding. 2011. The interaction between nesprins and sun proteins at the nuclear envelope is critical for force transmission between the nucleus and cytoskeleton. *J. Biol. Chem.* 286:26743–26753. https://doi.org/10.1074/jbc.M111.233700

Lovett, D.B., N. Shekhar, J.A. Nickerson, K.J. Roux, and T.P. Lele. 2013. Modulation of nuclear shape by substrate rigidity. *Cell. Mol. Bioeng.* 6:230–238. https://doi.org/10.1007/s12195-013-0270-2

Luxton, G.W., E.R. Gomes, E.S. Folker, E. Vintinner, and G.G. Gundersen. 2010. Linear arrays of nuclear envelope proteins harness retrograde actin flow for nuclear movement. *Science.* 329:956–959. https://doi.org/10.1126/science.1189072

Luxton, G.W., E.R. Gomes, E.S. Folker, H.J. Worman, and G.G. Gundersen. 2011. TAN lines: A novel nuclear envelope structure involved in nuclear positioning. *Nucleus.* 2:173–181. https://doi.org/10.4161/nucl.2.3.16243

Lyman, S.K., T. Guan, J. Bednenko, H. Wodrich, and L. Gerace. 2002. Influence of cargo size on Ran and energy requirements for nuclear protein import. *J. Cell Biol.* 159:55–67. https://doi.org/10.1083/jcb.200204163

Mahajan, R., C. Delphin, T. Guan, L. Gerace, and F. Melchior. 1997. A small ubiquitin-related polypeptide involved in targeting RanGAP1 to nuclear pore complex protein RanBP2. *Cell.* 88:97–107. https://doi.org/10.1016/S0092-8674(00)81862-0

Mattaj, I.W., and L. Englmeier. 1998. Nucleocytoplasmic transport: The soluble phase. *Annu. Rev. Biochem.* 67:265–306. https://doi.org/10.1146/annurev.biochem.67.1.265

Matunis, M.J., E. Coutavas, and G. Blobel. 1996. A novel ubiquitin-like modification modulates the partitioning of the Ran-GTPase-activating protein RanGAP1 between the cytosol and the nuclear pore complex. *J. Cell Biol.* 135:1457–1470. https://doi.org/10.1083/jcb.135.6.1457

Munevar, S., Y. Wang, and M. Dembo. 2001. Traction force microscopy of migrating normal and H-ras transformed 3T3 fibroblasts. *Biophys. J.* 80:1744–1757. https://doi.org/10.1016/S0006-3495(01)76145-0

Neelam, S., T.J. Chancellor, Y. Li, J.A. Nickerson, K.J. Roux, R.B. Dickinson, and T.P. Lele. 2015. Direct force probe reveals the mechanics of nuclear homeostasis in the mammalian cell. *Proc. Natl. Acad. Sci. USA.* 112:5720–5725. https://doi.org/10.1073/pnas.1502111112

Niopek, D., D. Benzinger, J. Roensch, T. Draebing, P. Wehler, R. Eils, and B. Di Ventura. 2014. Engineering light-inducible nuclear localization signals for precise spatiotemporal control of protein dynamics in living cells. *Nat. Commun.* 5:4404. https://doi.org/10.1038/ncomms5404

Niopek, D., P. Wehler, J. Roensch, R. Eils, and B. Di Ventura. 2016. Optogenetic control of nuclear protein export. *Nat. Commun.* 7:10624. https://doi.org/10.1038/ncomms10624

O'Neil, D., H. Glowatz, and M. Schlumpberger. 2013. Ribosomal RNA depletion for efficient use of RNA-seq capacity. *Curr. Protoc. Mol. Biol.* Chapter 4:Unit 4.19. https://doi.org/10.1002/0471142727.mb0419s103

Panté, N., and M. Kann. 2002. Nuclear pore complex is able to transport macromolecules with diameters of about 39 nm. *Mol. Biol. Cell.* 13:425–434. https://doi.org/10.1091/mbc.01-06-0308

Randles, K.N., T. Lam, C.A. Sewry, M. Puckelwartz, D. Furling, M. Wehnert, E.M. McNally, and G.E. Morris. 2010. Nesprins, but not sun proteins,

switch isoforms at the nuclear envelope during muscle development. *Dev. Dyn.* 239:998–1009. https://doi.org/10.1002/dvdy.22229

Ransom, J.T. 1995. Mechanism of action of mycophenolate mofetil. *Ther. Drug Monit.* 17:681–684. https://doi.org/10.1097/00007691-199512000-00023

Ribbeck, K., and D. Görlich. 2001. Kinetic analysis of translocation through nuclear pore complexes. *EMBO J.* 20:1320–1330. https://doi.org/10.1093/emboj/20.6.1320

Ribbeck, K., U. Kutay, E. Paraskeva, and D. Görlich. 1999. The translocation of transportin-cargo complexes through nuclear pores is independent of both Ran and energy. *Curr. Biol.* 9:47–50. https://doi.org/10.1016/S0960-9822(99)80046-3

Ribbeck, K., G. Lipowsky, H.M. Kent, M. Stewart, and D. Görlich. 1998. NTF2 mediates nuclear import of Ran. *EMBO J.* 17:6587–6598. https://doi.org/10.1093/emboj/17.22.6587

Rosenbluh, J., H. Xu, W. Harrington, S. Gill, X. Wang, F. Vazquez, D.E. Root, A. Tsherniak, W.C. Hahn, et al. 2017. Complementary information derived from CRISPR Cas9 mediated gene deletion and suppression. *Nat. Commun.* 8:15403. https://doi.org/10.1038/ncomms15403

Roux, K.J., M.L. Crisp, Q. Liu, D. Kim, S. Kozlov, C.L. Stewart, and B. Burke. 2009. Nesprin 4 is an outer nuclear membrane protein that can induce kinesin-mediated cell polarization. *Proc. Natl. Acad. Sci. USA.* 106:2194–2199. https://doi.org/10.1073/pnas.0808602106

Schwoebel, E.D., T.H. Ho, and M.S. Moore. 2002. The mechanism of inhibition of Ran-dependent nuclear transport by cellular ATP depletion. *J. Cell Biol.* 157:963–974. https://doi.org/10.1083/jcb.200111077

Sharma, R., and M.W. Hetzer. 2023. Disulfide bond in SUN2 regulates dynamic remodeling of LINC complexes at the nuclear envelope. *Life Sci. Alliance.* 6:e202302031. https://doi.org/10.26508/lsa.202302031

Smith, A.E., B.M. Slepchenko, J.C. Schaff, L.M. Loew, and I.G. Macara. 2002. Systems analysis of Ran transport. *Science.* 295:488–491. https://doi.org/10.1126/science.1064732

Solon, J., I. Levental, K. Sengupta, P.C. Georges, and P.A. Janmey. 2007. Fibroblast adaptation and stiffness matching to soft elastic substrates. *Biophys. J.* 93:4453–4461. https://doi.org/10.1529/biophysj.106.101386

Steggerda, S.M., B.E. Black, and B.M. Paschal. 2000. Monoclonal antibodies to NTF2 inhibit nuclear protein import by preventing nuclear translocation of the GTPase Ran. *Mol. Biol. Cell.* 11:703–719. https://doi.org/10.1091/mbc.11.2.703

Strope, T.A., C.J. Birky, and H.M. Wilkins. 2022. The role of bioenergetics in neurodegeneration. *Int. J. Mol. Sci.* 23:9212. https://doi.org/10.3390/ijms23169212

Talamas, J.A., and M.W. Hetzer. 2011. POM121 and Sun1 play a role in early steps of interphase NPC assembly. *J. Cell Biol.* 194:27–37. https://doi.org/10.1083/jcb.201012154

Tan, P.S., I.V. Aramburu, D. Mercadante, S. Tyagi, A. Chowdhury, D. Spitz, S.L. Shammas, F. Gräter, and E.A. Lemke. 2018. Two differential

binding mechanisms of FG-nucleoporins and nuclear transport receptors. *Cell Rep.* 22:3660–3671. https://doi.org/10.1016/j.celrep.2018.03.022

Tse, J.M., G. Cheng, J.A. Tyrrell, S.A. Wilcox-Adelman, Y. Boucher, R.K. Jain, and L.L. Munn. 2012. Mechanical compression drives cancer cells toward invasive phenotype. *Proc. Natl. Acad. Sci. USA.* 109:911–916. https://doi.org/10.1073/pnas.1118910109

Wawrzyniak, J.A., A. Bianchi-Smiraglia, W. Bshara, S. Mannava, J. Ackroyd, A. Bagati, A.R. Omilian, M. Im, N. Fedtsova, J.C. Miecznikowski, et al. 2013. A purine nucleotide biosynthesis enzyme guanosine monophosphate reductase is a suppressor of melanoma invasion. *Cell Rep.* 5:493–507. https://doi.org/10.1016/j.celrep.2013.09.015

Wilhelmsen, K., S.H. Litjens, I. Kuikman, N. Tshimbalanga, H. Janssen, I. van den Bout, K. Raymond, and A. Sonnenberg. 2005. Nesprin-3, a novel outer nuclear membrane protein, associates with the cytoskeletal linker protein plectin. *J. Cell Biol.* 171:799–810. https://doi.org/10.1083/jcb.200506083

Williams, T., L.H. Ngo, and V.O. Wickramasinghe. 2018. Nuclear export of RNA: Different sizes, shapes and functions. *Semin. Cell Dev. Biol.* 75:70–77. https://doi.org/10.1016/j.semcdb.2017.08.054

Wu, J., I.A. Kent, N. Shekhar, T.J. Chancellor, A. Mendonca, R.B. Dickinson, and T.P. Lele. 2014. Actomyosin pulls to advance the nucleus in a migrating tissue cell. *Biophys. J.* 106:7–15. https://doi.org/10.1016/j.bpj.2013.11.4489

Yeung, T., P.C. Georges, L.A. Flanagan, B. Marg, M. Ortiz, M. Funaki, N. Zahir, W. Ming, V. Weaver, and P.A. Janmey. 2005. Effects of substrate stiffness on cell morphology, cytoskeletal structure, and adhesion. *Cell Motil. Cytoskeleton.* 60:24–34. https://doi.org/10.1002/cm.20041

Yokoyama, N., N. Hayashi, T. Seki, N. Panté, T. Ohba, K. Nishii, K. Kuma, T. Hayashida, T. Miyata, U. Aebi, et al. 1995. A giant nucleopore protein that binds Ran/TC4. *Nature.* 376:184–188. https://doi.org/10.1038/376184a0

Zhang, Q., V. Narayanan, K.L. Mui, C.S. O'Bryan, R.H. Anderson, B. Kc, J.I. Cabe, K.B. Denis, S. Antoku, K.J. Roux, et al. 2019. Mechanical stabilization of the glandular acinus by linker of nucleoskeleton and cytoskeleton complex. *Curr. Biol.* 29:2826–2839.e4. https://doi.org/10.1016/j.cub.2019.07.021

Zhang, Q., J.N. Skepper, F. Yang, J.D. Davies, L. Hegyi, R.G. Roberts, P.L. Weissberg, J.A. Ellis, and C.M. Shanahan. 2001. Nesprins: A novel family of spectrin-repeat-containing proteins that localize to the nuclear membrane in multiple tissues. *J. Cell Sci.* 114:4485–4498. https://doi.org/10.1242/jcs.114.24.4485

Zimmerli, C.E., M. Allegretti, V. Rantos, S.K. Goetz, A. Obarska-Kosinska, I. Zagoriy, A. Halavatyi, G. Hummer, J. Mahamid, J. Kosinski, and M. Beck. 2021. Nuclear pores dilate and constrict in cellulo. *Science.* 374:eabd9776. https://doi.org/10.1126/science.abd9776
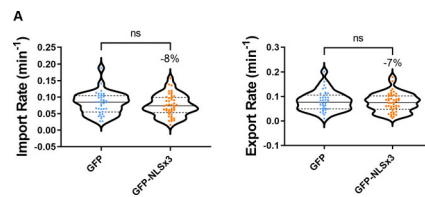
Supplemental material

Figure S1. **Assessing the impact of overexpression of an NLS-containing protein on NCT. (A)** Import and export rates of BJ-5ta cells expressing LINuS and GFP (n = 38) or GFP-NLSx3 (n = 46). Results are from two independent replicates. Significance was calculated using unpaired *t* test. ns P > 0.05.
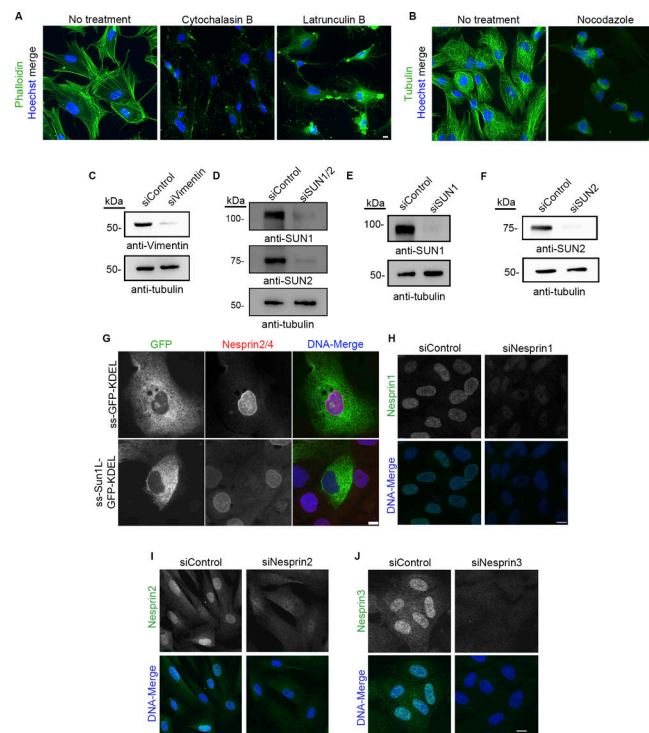

Figure S2. **Validation of drug treatments and LINC complex disruption. (A)** IF validation of actin-cytoskeleton disruption in BJ-5ta cells treated with either cytochalasin B or latrunculin. Phalloidin (green) was used as a marker for F-actin. **(B)** IF validation of tubulin disruption in BJ-5ta cells treated with nocodazole. **(C–F)** Western blot validation of siRNA knockdowns of (C) vimentin (D) SUN1 and SUN2 (SUN1/2), (E) SUN1, or (F) SUN2 knockdown in BJ-5ta cells. Tubulin was used as a loading control. **(G)** Representative fluorescence images of MCF10A cells transiently transfected with ss-GFP-KDEL or ss-SUN1L-GFP-KDEL (green) probed for Nesprin2/4 (red) to assess loss of nesprins from the NE that is indicative of LINC complex perturbation. **(H–J)** Representative fluorescence images of BJ-5ta cells depleted of (H) Nesprin1, (I) Nesprin2, or (J) Nesprin3 (green), labeled with respective antibodies. Hoescht was used to visualize DNA (blue). Scale bars 10 μm. Source data are available for this figure: SourceData FS2.
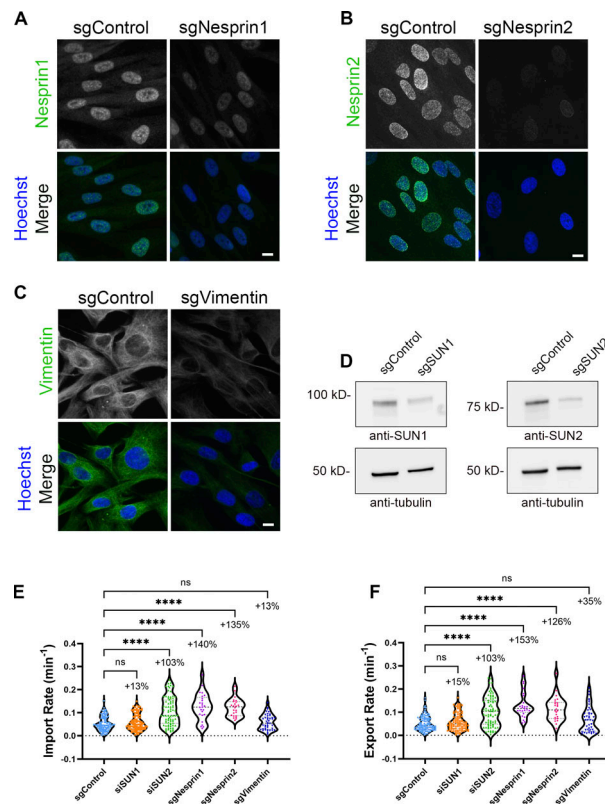
Figure S3. **Validation of LINC perturbation on NCT using CRISPR interference. (A–C)** IF validation of transient loss of LINC proteins in BJ-5ta cells stably expressing dCas9-KRAB-IRES-LINuS transfected with guide RNAs against (A) Nesprin1 (sgNesprin1), (B) Nesprin2 (sgNesprin2), or (C) Vimentin (sgVimentin). Scale bars 10 μm. **(D)** Western blot validation of the transient loss of SUN1 (sgSUN1) or SUN2 (sgSUN2) proteins in BJ-5ta cells stably expressing dCas9-KRAB-IRES-LINuS. Tubulin was used as a loading control. **(E and F)** Import and export rates of BJ-5ta cells expressing KRAB-dCas9-IRES-LINuS (CRISPRi) and transfected with gRNAs against SUN1 (sgSUN1), SUN2 (sgSUN2), Nesprin1 (sgNesprin1), Nesprin2 (sgNesprin2), and vimentin (sgVimentin). sgControl ($n = 109$), sgSUN1 ($n = 106$), sgSUN2 ($n = 80$); three independent replicates. sgVimentin ($n = 42$), sgNesprin1 ($n = 25$), sgNesprin2 ($n = 24$); two independent replicates. Significance was calculated using one-way ANOVA with Dunnett's post hoc. ns $P > 0.05$, $P*** < 0.001$, $P**** < 0.0001$. Source data are available for this figure: SourceData FS3.
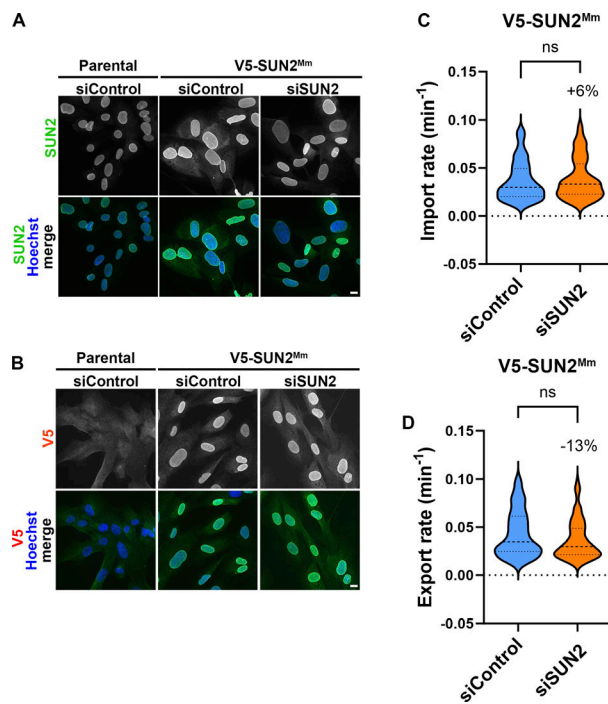
Figure S4. **Validation of siSUN2 specificity. (A and B)** Representative fluorescence images of BJ-5ta cells stably expressing LINuS (parental) or co-expressing LINuS and a V5-tagged mouse SUN2 (V5-SUN2^{Mm}) and transfected with either siControl or siSUN2 to transiently knockdown endogenous SUN2. Cells were subsequently labeled with antibodies against SUN2 (A) or V5 (B) to validate the resistance of exogenous mouse SUN2 to human SUN2 siRNAs. **(C and D)** Import and export rates of BJ-5ta cells stably expressing LINuS and V5-SUN2^{Mm} and depleted of endogenous SUN2 (siControl n = 94, siSUN2 n = 91). Results are from two independent replicates. Scale bar 10 μm.
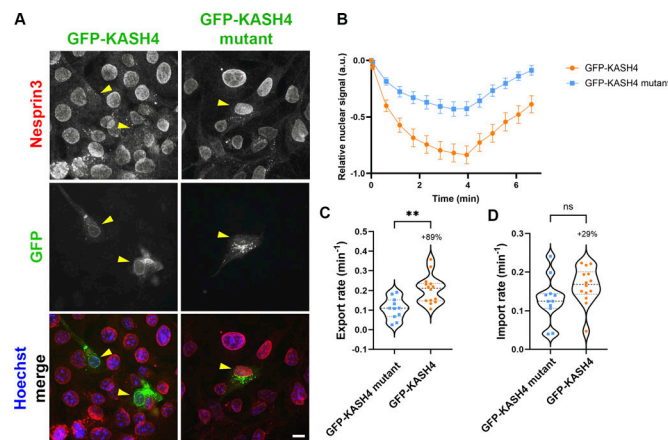

Figure S5. **Validation of LINC perturbation on NCT using the LEXY reporter. (A)** Representative fluorescence images of MEFs transfected with either GFP-KASH4 or GFP-KASH4 mutant that cannot bind the SUN domain (yellow arrows) labeled with antibodies against Nesprin3 to validate loss of nesprin from the NE in the presence of dominant-negative GFP-KASH4 but not the mutant control. Scale bar 10 μm. **(B)** Quantification of LEXY nuclear localization during photoactivation in MEFs transiently transfected with either GFP-KASH4 or GFP-KASH4 mutant to disrupt the LINC complex (GFP-KASH4 n = 14, GFP-KASH4 mutant n = 11). **(C and D)** Import and export rates from A.

Video 1. **GFP-Ran localization in control cells.** Video of untreated BJ-5ta cells stably expressing GFP-Ran. Images were captured at 40× every 10 s for 30 min and displayed at 9 frames/s. Images from this video are shown in Fig. 8 E.

Video 2.   **GFP-Ran localization shifts to the cytoplasm following cytochalasin B treatment.** Video of BJ-5ta cells stably expressing GFP-Ran following addition of 20 µM cytochalasin B. Images were captured at 40× every 10 s for 30 min and displayed at 9 frames/s. Images from this video are shown in Fig. 8 E.